Stem Cell Reports
Article

ISSCR

OPEN ACCESS

Astrocytic reactivity triggered by defective autophagy and metabolic failure causes neurotoxicity in frontotemporal dementia type 3

Abinaya Chandrasekaran,[1,15] Katarina Stoklund Dittlau,[1,15] Giulia I. Corsi,[1,2] Henriette Haukedal,[1] Nadezhda T. Doncheva,[1,2,3] Sarayu Ramakrishna,[4,5] Sheetal Ambardar,[4,6] Claudia Salcedo,[7] Sissel I. Schmidt,[8] Yu Zhang,[9] Susanna Cirera,[1] Maria Pihl,[1] Benjamin Schmid,[10] Troels Tolstrup Nielsen,[11] Jørgen E. Nielsen,[11] Miriam Kolko,[7,12] Julianna Kobolák,[14] András Dinnyés,[14] Poul Hyttel,[1] Dasaradhi Palakodeti,[4] Jan Gorodkin,[1,2] Ravi S. Muddashetty,[4] Morten Meyer,[8,13] Blanca I. Aldana,[7] and Kristine K. Freude[1,*]

[1]Department of Veterinary and Animal Sciences, Faculty of Health and Medical Sciences, University of Copenhagen, Frederiksberg 1870, Denmark
[2]Center for Non-coding RNA in Technology and Health, University of Copenhagen, Frederiksberg 1871, Denmark
[3]Novo Nordisk Foundation Center for Protein Research, University of Copenhagen, Copenhagen 2200, Denmark
[4]Institute for Stem Cell Science and Regenerative Medicine, Bangalore 560065, India
[5]The University of Trans-Disciplinary Health Sciences and Technology, Bangalore 560064, India
[6]National Center for Biological Sciences, Tata Institute of Fundamental Research, Bangalore 560065, India
[7]Department of Drug Design and Pharmacology, Faculty of Health and Medical Sciences, University of Copenhagen, Copenhagen 2100, Denmark
[8]Department of Neurobiology Research, Institute of Molecular Medicine, University of Southern Denmark, 5000 Odense, Denmark
[9]Department of Experimental Medical Science, Wallenberg Center for Molecular Medicine and Lund Stem Cell Center, Lund University, Lund 22184, Sweden
[10]Bioneer A/S, Hørsholm 2970, Denmark
[11]Danish Dementia Research Centre, Rigshospitalet, University of Copenhagen, Copenhagen 2100, Denmark
[12]Department of Ophthalmology, Copenhagen University Hospital, Rigshospitalet, Copenhagen 2100, Denmark
[13]Department of Neurology, Odense University Hospital, 5000 Odense, Denmark
[14]BioTalentum Ltd; 2100 Gödöllő, Hungary
[15]These author contributed equally
*Correspondence: kkf@sund.ku.dk
https://doi.org/10.1016/j.stemcr.2021.09.013

SUMMARY

Frontotemporal dementia type 3 (FTD3), caused by a point mutation in the charged multivesicular body protein 2B (CHMP2B), affects mitochondrial ultrastructure and the endolysosomal pathway in neurons. To dissect the astrocyte-specific impact of mutant CHMP2B expression, we generated astrocytes from human induced pluripotent stem cells (hiPSCs) and confirmed our findings in CHMP2B mutant mice. Our data provide mechanistic insights into how defective autophagy causes perturbed mitochondrial dynamics with impaired glycolysis, increased reactive oxygen species, and elongated mitochondrial morphology, indicating increased mitochondrial fusion in FTD3 astrocytes. This shift in astrocyte homeostasis triggers a reactive astrocyte phenotype and increased release of toxic cytokines, which accumulate in nuclear factor kappa b (NF-κB) pathway activation with increased production of CHF, LCN2, and C3 causing neurodegeneration.

INTRODUCTION

Frontotemporal dementia type 3 (FTD3) is a rare heterozygous early-onset form of frontotemporal dementia (Skibinski et al., 2005). The disease is caused by a single nucleotide substitution in the CHMP2B gene resulting in a C-terminal truncated protein (Lindquist et al., 2008). CHMP2B is a central component of the endosomal-sorting complex required for transport-III (ESCRT-III). The mutation is associated with impairment of the endolysosomal pathway, leading to accumulation of early-stage endosomes, and culminates in neuronal death and gliosis of the surrounding tissue (Urwin et al., 2010; Zhang et al., 2017).

Astrocytes are one of the most abundant non-neuronal cell types of the central nervous system, displaying remarkable heterogeneity both in morphology and function (Azevedo et al., 2009). Previous research has shown that astrocytes participate in numerous functions, such as the formation of neuronal networks, production of neurotrophic factors, recycling of neurotransmitters, and maintenance of homeostasis via detoxification and nutritional distribution (Haim et al., 2015). Glial cell pathology, manifested in astrocyte reactivity, has been reported for Alzheimer disease (AD), Huntington disease, and amyotrophic lateral sclerosis (ALS) (Osborn et al., 2016; Qian et al., 2017).

Autophagy is intracellular degradation of damaged organelles such as mitochondria, protein aggregates, and long-lived proteins for subsequent recycling of usable subunits (Nakamura and Yoshimori, 2017). The autophagy pathway is highly selective and often subdivided based on its engulfed material, such as mitophagy facilitating the breakdown of damaged mitochondria (Ding and Yin, 2012). An important connection between the endolysosomal pathway and autophagy is the fusion between late endosomes and autophagosomes into amphisomes, which further fuse with lysosomes (Jäger et al., 2004). This part of the process is an important feature in FTD3 pathology as impairment of the amphisome formation due to

ESCRT-III dysfunction has been demonstrated to result in autophagosome and endosome accumulation (Lee et al., 2007). P62 is a soluble cytosolic protein, incorporating polyubiquitinated cargo into autophagosomes. Several studies have provided evidence that P62 expression is increased in neurodegenerative diseases such as ALS and frontotemporal lobar degeneration (FTLD) (Rea et al., 2014). Our previous findings revealed accumulation of P62 in the S100β-positive glial cell population among human induced pluripotent stem cell (hiPSC)-derived FTD3 neurons (Zhang et al., 2017), which triggered the current investigation of autophagic alterations in FTD3 astrocytes and understanding of the mechanism contributing to FTD3 pathology.

RESULTS

Efficient generation and characterization of hiPSC-derived FTD3 astrocytes

Astrocytes were differentiated from hiPSC lines derived from two related patients with CHMP2B mutation (FTD3 patient 1 and FTD3 patient 2), and their corresponding isogenic control, in which the mutation was corrected via CRISPR/Cas9 gene editing (isogenic control 1 and isogenic control 2, respectively). Additionally, two CRISPR/Cas9 knockin cell lines were generated carrying the same CHMP2B mutation (homozygous and heterozygous; Table S1). All FTD3-hiPSCs and control-hiPSCs were successfully differentiated into astrocytes with comparable efficiencies following a modified version of an established protocol (Shaltouki et al., 2013) (Figure 1A). All astrocyte cultures expressed characteristic astrocyte markers: transcription factor SOX-9 (SOX9), protein S100-B (S100β), and aquaporin-4 (AQP4) validated by immunocytochemistry (ICC) (Figure 1B) at 7 weeks of differentiation. No obvious difference was observed, indicating that the CHMP2B mutation has no effect on the differentiation capacity towards astrocytes. On average, 85% of astrocytes were S100β, AQP4, and SOX9 positive (Figures 1C–1E).

FTD3 astrocytes show increased and imbalanced autophagy

Impaired autophagy has been implicated in the pathogenesis of ALS and FTD3 (Edens et al., 2016). Due to their classical functions of delivering autophagic cargo into autophagosomes, P62 and LC3 expression is generally considered to correlate with the level of autophagic degradation. Our results uncovered high ICC expression of both proteins in FTD3 astrocytes compared with controls, indicative of an accumulation of autophagosomes and possible impairment of autophagy (Figures 2A–2C, S2–S4). An increase in the autophagic flux was confirmed via western blot (WB) (Figures 2D and 2E).

To further visualize the changes in autophagy, we performed transmission electron microscopy (TEM). TEM analyses of FTD3 astrocytes displayed double-membraned autophagosomes with increased electron-dense content of engulfed cellular components and organelles, indicating accumulation of un-processed material, reflecting a possible impaired amphisome formation and/or lysosomal fusion. In contrast, isogenic control lines presented electron-lucent autophagosomes, potentially representing early autophagosomes and secondary lysosomes (Figures 2F and S4). Consequently, we investigated if this impairment of autophagy-mediated clearance is caused by the inability to transport autophagosomes to the lysosomes, as seen with endosomes in FTD3 neurons (Urwin et al., 2010). Co-labeling for P62 and RAB7 (Figure 2A, middle column) revealed an increase in colocalization in FTD3 astrocytes compared with controls (Figures 2G and 2H), which suggests that RAB7-mediated transport of autophagosomes is increased but not impaired in FTD3 astrocytes. To further examine the autophagosome-lysosome fusion process, we performed ICC for P62 and lysosomal associated membrane protein 1 (LAMP1) (Figure 2A, right column). Puncta quantifications revealed a specific increase in LAMP1 colocalization with P62 in FTD3 astrocytes, indicating an increased formation of autolysosomes in the mutated astrocytes (Figures 2I and 2J) (Pugsley, 2017), further validated by WB (Figures 2K and 2L). To further substantiate the autophagy abnormalities in human FTD3 astrocytes, we analyzed autophagy-related genes in brains obtained from a transgenic mouse model overexpressing human CHMP2B Intron5 mutation ($CHMP2B^{intron5}$ mice). The results showed an increase in the expression of autophagy genes *p62*, *Rab7*, and *Lamp1* in $CHMP2B^{intron5}$ mice via qPCR and WB (Figures 2M–2Q), resembling he increased autophagy activity in iPSC-derived astrocytes.

Since no obvious impairments were found in the transport and fusion of autophagosomes with lysosomes, we treated the astrocytes with two different concentrations (200 nM and 500 nM) of rapamycin, a potent inducer of autophagy, in order to further activate and promote the clearance of autophagosomes in the FTD3 astrocytes. Overall, this attempt was unsuccessful, as it changed the abundance of neither the P62 and LC3B punctae (Figures S2–S4) nor the RAB7-mediated transport and LAMP1-mediated lysosomal fusion, which suggests that autophagy is impaired in one or more unidentified steps of the process. Only in the homozygous line did we observe a reduction in the number of P62, RAB7, and LAMP1 punctae as well as the colocalization of P62 and LAMP1. The 200 nM treatment did also lower LC3B in FTD3 patient 1 compared with its control; however, we did not observe this in the other FTD3 lines. In order to further investigate if mitophagy

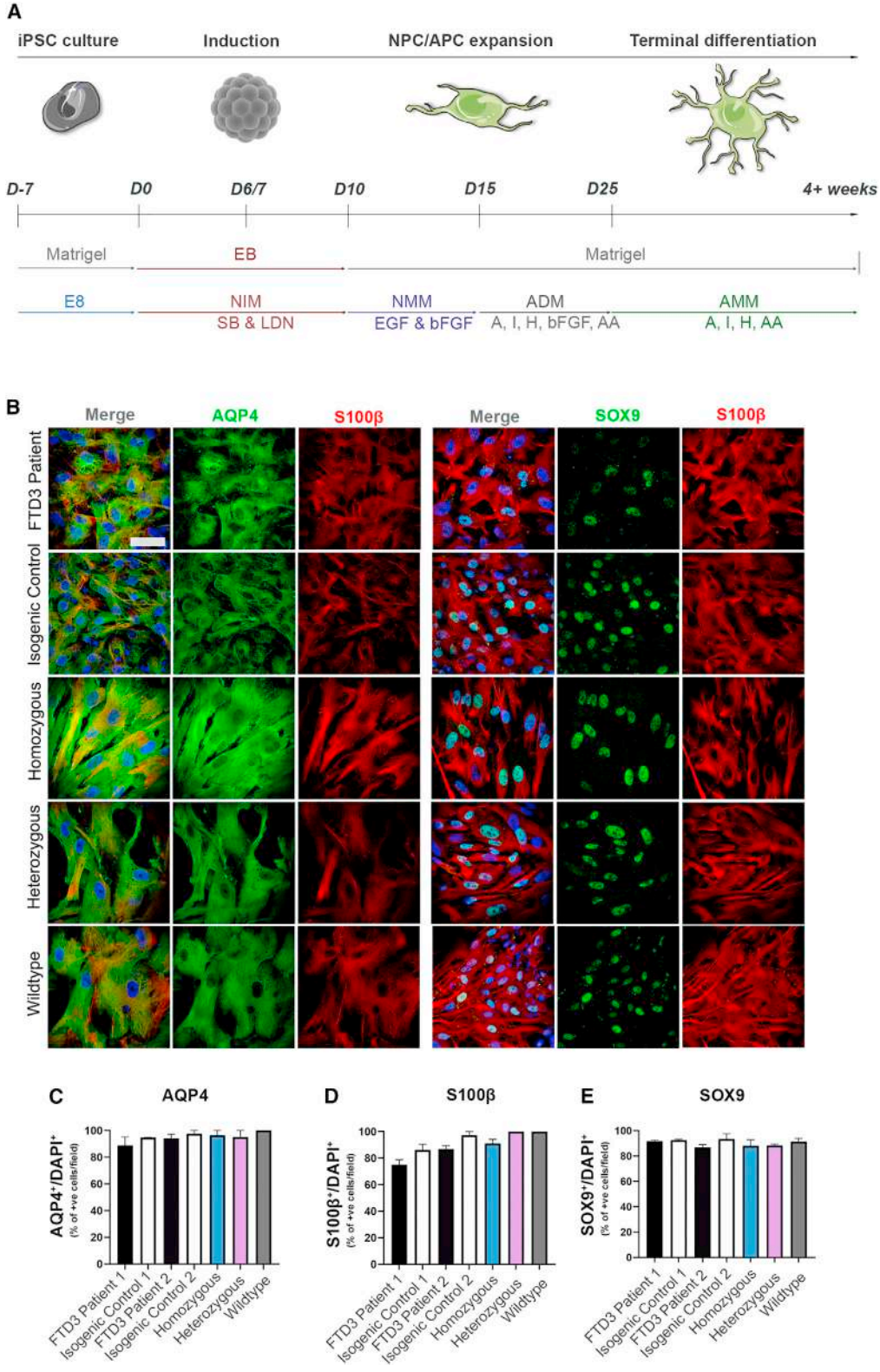

(legend on next page)

impairments are causing the autophagosome accumulations, we performed ICC using TOM20 (mitochondrial marker) and LAMP1. We found that FTD3 lines promoted mitochondria-LAMP1 colocalization, indicating an upregulation in the mitophagic turnover of mitochondria (Figures S4A–S4C).

FTD3 astrocytes display impaired mitochondrial dynamics and function

Next we investigated if the autophagic defects in our FTD3 astrocytes lead to accumulation of dysfunctional mitochondria and enhanced production of reactive oxidative species (ROS) linked to hampered respiratory function. Assessment of ROS revealed increased levels of oxidative stress in FTD3 astrocytes, substantiating that mitochondria function and turnover are affected (Figure 3A). Prompted by our observations of increased ROS, we tested the mitochondrial function by assessing their basal respiration rate and ATP-linked respiration. Our real-time bioenergetics analyses uncovered a reduced basal and maximal respiration as well as decreased oxygen consumption linked to ATP production in the FTD3 astrocytes compared with controls (Figure 3B). Furthermore, our RNA sequencing (RNA-seq) analyses revealed altered expression levels of genes related to oxidative stress in FTD3 astrocytes (Table S2). For instance Thioredoxin Reductase 2 (*TXNRD2*), known to scavenge ROS in mitochondria (Lu and Holmgren, 2012), was downregulated in FTD3 astrocytes. This is in agreement with a recent study reporting that TXNRD2 deficiency causes increased ROS levels, affecting the oxidative phosphorylation system, and results in reduced ATP availability (Holzerova et al., 2016). Similarly, Mitogen-Activated Protein Kinase 9 (*MAP3K9*), an essential component of the MAP kinase signal transduction pathway, was downregulated in FTD3 astrocytes. Next, we investigated whether mitochondria dysfunction and increased oxidative stress affect cell viability. WB analysis for cleaved caspase 3 (CASP3), did not reveal increased apoptotic activity in FTD3 astrocytes (Figure 3C). Even though astrocyte survival is not affected at this point, our data indicate an impairment of handling oxidative stress in FTD3 astrocytes. Oxidative stress has been linked to the formation of stress granules (SGs), and a key component of stress granules is the prion-related RNA-binding protein, T cell intracellular antigen-1 (TIA-1), which was examined via ICC. Indeed, the number of SGs was increased and more scattered in FTD3 astrocytes compared with controls, indicating increased SG formation as a direct result of impaired autophagy (Silva et al., 2019) (Figures 3D and 3E).

Mitochondrial dynamics in astrocytes are far less studied compared with neurons but could play an important role in the FTD3 disease mechanism. We examined mitochondrial networks using MitoTracker Red CMXRos followed by high-resolution morphology studies via TEM. MitoTracker experiments revealed that FTD3 astrocytes display an interconnected meshwork of elongated mitochondria compared with their controls, indicative of decreased fission and increased fusion (Figures 3F and 3G). Our TEM results confirmed excessively elongated mitochondria in FTD3 astrocytes (Figure 3H). TEM quantitative analysis revealed a reduction in relative mitochondria to cytoplasm area ratio in FTD3 patient 1 and heterozygous induced astrocytes (Figure S4G). The same tendency was observed in FTD3 patient 2 and homozygous induced astrocytes indicating a reduction in total mitochondria number correlating with the observation of increased fusion and reduced fission. Furthermore, a significant increase in relative individual mitochondria area was observed in FTD3 patient 1, possibly due to increased fusion and mitochondria elongation (Figure S4F).

Strikingly, RNA-seq analysis revealed differential expression of genes functionally linked to mitochondrial fission/fusion processes (Table S2). Dynamin 3 (*DNM3*), a member of the dynamin superfamily, was upregulated in FTD3 astrocytes (validated by qPCR; Figure 3I). The dynamin-related GTPase DNM3 controls mitochondrial morphology by recruiting dynamin-related protein 1 (DRP1), and mutation in DNM3 interferes with the mitochondria morphology (Fonseca et al., 2019). In addition, BCL2 Interacting Protein 3 (*BNIP3*), a regulator of mitochondrial fission/fusion dynamics (Autret and Martin, 2010), was reduced in FTD3 patient astrocytes (Table S2). Furthermore, expression of the kinase insert domain receptor (*KDR*), whose silencing was shown to increase the mitochondrial membrane permeability (Zhang et al., 2014), was reduced (Table S2) in FTD3 astrocytes, further supporting unbalanced fission-fusion events.

Next we investigated if key regulators of mitochondrial fission and fusion processes are affected. In accordance with the observed mitochondria elongation phenotype, we observed increased optic atrophy 1 (OPA1) and mitofusin 1 (MFN1) expression levels in FTD3 patient astrocytes and CHMP2B^{intron5} mice brains (Yu et al., 2020). A similar

Figure 1. Generation and characterization of hiPSC-derived astrocytes

(A) Schematic of astrocyte differentiation protocol.

(B) Representative ICC images of AQP4, S100β, and SOX9. Scale bar, 25 μm.

(C–E) Quantifications of AQP4, S100β, and SOX9 expression. Mean ± SEM of three independent experiments. One-way ANOVA with Tukey multiple comparisons test; *p < 0.05. See also Figure S1.

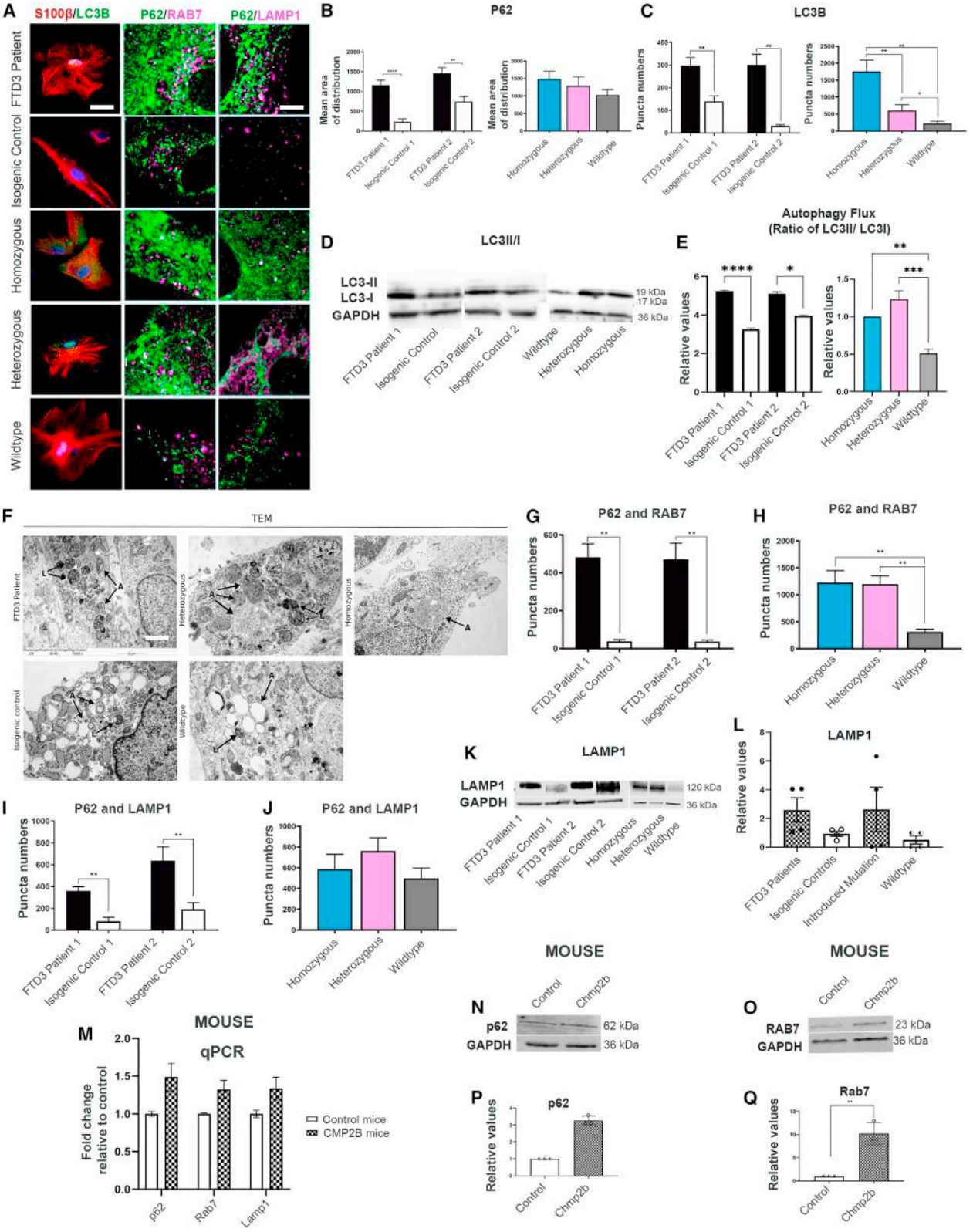

(legend on next page)

trend in the expression level changes of fission protein 1 (FIS1) was observed in both FTD3 patient astrocytes and in CHMP2B^{intron5} mice brain (Figures 3J and 3K), which has been seen to cause mitochondrial elongation (Yoon et al., 2003). The evidence of mitochondria dysfunction is further supported by our RNA-seq data showing downregulation of additional mitochondrial-related genes in FTD3 astrocytes (Figure 3L; Table S2). Ursodeoxycholic acid (UDCA) has been proved to rescue apoptotic cascades downstream of autophagic and endosomal perturbations in CHMP2B^{Intron5} expressing *Drosophila* (West et al., 2020). In addition, it has proved to rescue mitochondrial defects in *parkin*-deficient neurons in iPSC-derived models (Mortiboys et al., 2013). Treatment with 50 nM UDCA was sufficient to reduce ROS in FTD3 astrocytes compared with controls (Figure 3A). However, there was no effect of UDCA on mitochondrial respiration or on ATP coupled respiration (data not shown). Collectively, our results suggest that the impaired mitochondrial function and antioxidant capacity of FTD3 astrocytes contribute to both metabolic and oxidative stress.

FTD3 astrocytes display glucose and acetate hypometabolism

The observed functional impairments of mitochondria in FTD3 astrocytes led us to investigate whether these cause metabolic deficiencies. Glucose and acetate oxidative metabolism is closely linked to mitochondria function via the tricarboxylic acid (TCA) cycle, which provides high-energy intermediates for the electron transport chain (ETC) leading to ATP production (McKenna et al., 2012). To provide detailed insights into relevant pathways of glucose and acetate metabolism, we used ^{13}C-labeled energy substrates and mass spectrometry (GC-MS) analysis to quantify ^{13}C incorporation in cellular metabolites. Figures 4A–4F shows the percentage distribution of ^{13}C labeling in fully labeled (M+3) lactate and alanine arising from direct metabolism of [U-^{13}C] glucose (2.5 mM). We observed a decrease in labeled lactate and alanine in FTD3 astrocytes compared with controls. However, the difference in labeled alanine found in FTD3 patient 2 did not reach statistical significance compared with isogenic control 2 (Figure 4E). Interestingly, the ^{13}C labeling of most of the amino acids and metabolites, except for glutamate (FTD3 patient 1; Figure 4G), obtained from a first turn of the TCA cycle in FTD3 astrocytes was lower than their controls, suggesting an overall decreased TCA cycle activity in FTD3 astrocytes (Figures 4G–4I). In line with our observation, RNA-seq revealed that numerous genes related to TCA and ETC are downregulated in FTD3 astrocytes (Table S2, Figure 4M). Specifically, genes of the mitochondrial NADH-ubiquinone oxidoreductase chain family (*MT-ND1*, *MT-ND2*, and *MT-ND3*) and mitochondrial encoded cytochrome C oxidases (*MT-CO2* and *MT-CO3*), which are implicated in oxidative phosphorylation, were downregulated. This indicates an impaired glucose metabolism resulting in decreased ATP synthesis, which is in line with our observation of hampered mitochondrial respiration.

Next, astrocytes were incubated in medium containing [1, 2-^{13}C] acetate (2.5 mM) and unlabeled glucose (2.5 mM). In astrocytes, [1, 2-^{13}C] acetate (M+2) enters the TCA cycle as acetyl coenzyme A, which in a first turn of the TCA cycle condenses with oxaloacetate to form double-labeled citrate (M+2). This TCA cycle intermediate is further metabolized, giving rise to α-ketoglutarate, fumarate, and malate (M+2). Aspartate (M+2) is formed from oxaloacetate (M+2). All metabolites evaluated were decreased in FTD3 astrocytes compared with respective controls (Figures 4J–4L), which supports the observed energy hypometabolism. Reduced expression of *MT-ND* genes could explain the observed dysfunction of mitochondrial respiratory chain with subsequent reduced ATP production (Zhao et al., 2011). In addition, we found mitochondrial uncoupling protein 2 and 3 (*UCP2* and *UCP3*) genes, which code for transporter proteins that create proton leaks across the inner mitochondrial membrane, to be downregulated in FTD3 astrocytes. Astrocytes take up and process most of synaptic glutamate (Danbolt, 2001). We

Figure 2. FTD3 astrocytes display autophagy changes

(A) Representative images of LC3B and S100β co-labeling of astrocytes (left column), P62 and RAB7 co-labeling of astrocytes (middle column), and P62 and LAMP1 co-labeling of astrocytes (right column) Scale bar, 25 μm (left column). Scale bar, 10 μm (middle and right column).

(B and C) P62 and LC3B puncta quantification.

(D and E) WB of autophagic flux (ratio of LC3II/I).

(F) TEM images of FTD3-specific accumulation of electron-dense autophagosomes indicated with black arrows. A, autophagosomes; L, autolysosomes. Scale bar, 2 μm.

(G and H) Puncta quantifications of P62 and RAB7 colocalization.

(I and J) Puncta quantifications of P62 and LAMP1 colocalization.

(K and L) WB of LAMP1.

(M–Q) Validation of CHMP2B^{intron5} mice versus control mice brain for autophagy via qPCR (M) and WB (N–Q). Mean ± SEM of three independent experiments. One-way ANOVA with Tukey multiple comparisons test; *p < 0.05, **p < 0.01, ***p < 0.001, and ****p < 0.0001. See also Figures S2–S4.

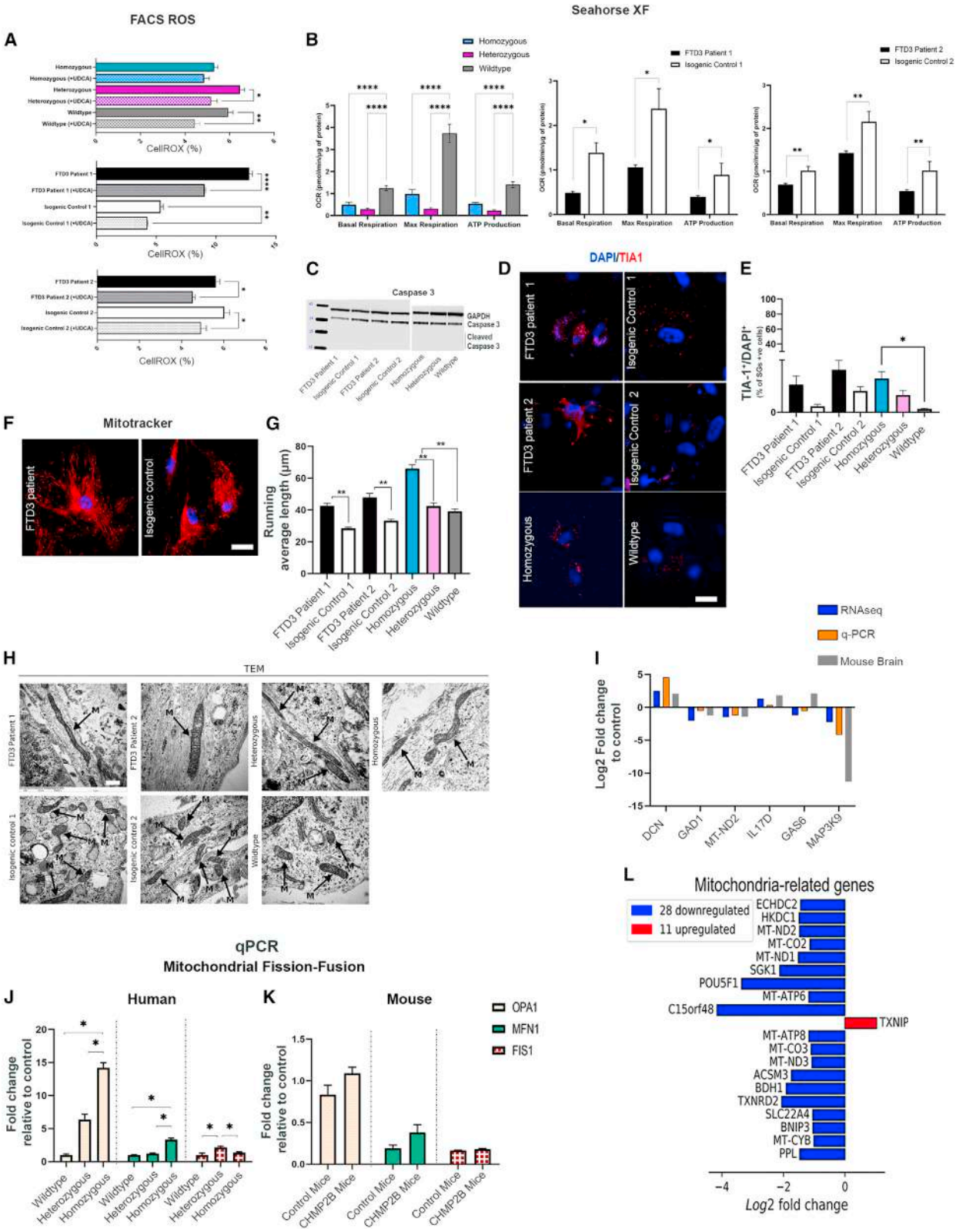

(legend on next page)

have recently shown that FTD3 astrocytes displayed increased glutamate uptake and metabolism (Aldana et al., 2020). Here, we observed a slight increase in the labeling in lactate in the FTD3 astrocytes when incubated with [U-^{13}C] glutamate and unlabeled glucose (Figures S5A–S5C), possibly reflecting the increased glutamate metabolism. Collectively, these results indicate decreased glucose and acetate metabolism associated with decreased TCA cycle activity in FTD3 astrocytes.

FTD3 astrocytes demonstrate increased reactivity

The homeostatic changes in FTD3 astrocytes could trigger conversion of resting astrocytes to reactive astrocytes contributing to the observed neurodegeneration and gliosis in FTD3 patients (Radford et al., 2015). To investigate astrocyte reactivity, we performed ICC using neutrophil gelatinase-associated lipocalin (LCN2) and glial fibrillary acidic protein (GFAP) as markers for reactive astrocytes (Lee et al., 2009b; Liddelow et al., 2017). Image analyses via puncta quantifications revealed an increase in LCN2 and GFAP expression in FTD3 patients' astrocytes compared with their controls, indicating increased numbers of reactive astrocytes (Figures 5A–5C). Surprisingly, GFAP expression was not increased in introduced mutation lines, contrary to the presence of all other disease phenotypes. Consistent with this, RNA-seq with FTD3 patient lines revealed upregulation of mitogen-activated protein kinase 1 (*MAP3K1*) in FTD3 astrocytes (Table S2). MAP3K1 is an inhibitor of nuclear factor kappa b kinase subunit beta (IKBKB), triggering phosphorylation and activation of nuclear factor kappa b (NF-κB) (Xia et al., 1998), which regulates genes implicated in immune responses (Lee et al., 1998). Supporting the transcriptome profile, the presence of phosphorylated NF-κB was validated by WB (Figures 5D and 5E). Even more intriguing, we found an upregulation of complement C3 (*C3*), fibulin 5 (*FBLN5*) and serpin family G member 1 (*SERPING1*) in FTD3 astrocytes (Table S2) via RNA-seq analysis. C3 and SERPING1 are regulators of the complement system, important for the innate immune response, and mutations in these genes have been implicated to induce toxic reactive astrocyte phenotypes in neurological diseases (Fraczek et al., 2011). To validate the RNA-seq expression changes on a protein level, we analyzed astrocyte reactivity via WB. Our results revealed increased protein expression of C3 in FTD3 astrocytes compared with their controls (Figures 5F and 5G). Additionally, we performed WB (Figures 5H–5K) and qPCR analysis (Figure 5L) of CHMP2B^{intron5} mice brains, revealing robust increase of C3 and Lcn2 and thereby confirming the astroglial phenotypes both *in vivo* and *in vitro*.

Cytokine secretion triggers reactive astrocytes to further secrete cytokines through an autoregulative loop

Cytokines are considered to be effectors of reactivity (Heneka et al., 2015). Specific cytokines such as interleukin (IL) 1 alpha, tumor necrosis factor alpha (TNFα), and complement component 1q subcomponent (C1q) are capable of inducing a reactive phenotype in astrocytes (Liddelow et al., 2017). Comparative analyses of secreted cytokines revealed that FTD3 astrocytes secreted higher levels of inflammatory-related proteins IL-6, IL-8, IL-13, TNFα, and IL-2 compared with controls (Figures 5M–5O and S5D–S5F). Likewise, we observed a similar pattern of expression for IL-6 via qPCR in CHMP2B^{intron5} mice brains demonstrating a coordinated immune response (Figure 5L). Additionally, RNA-seq showed enrichment of differentially expressed genes involved in inflammatory response (Gene Ontology [GO]: 0006954) in the FTD3 astrocytes (Table S3). A number of these genes are engaged in the NF-κB and TNF signaling pathways (KEGG hsa04064 and hsa04668), such as Vascular Cell Adhesion Molecule 1 (*VCAM1*), CD40 molecule (*CD40*), Lymphocyte Antigen 96 (*LY96*), Phosphatidylinositol-4,5-Bisphosphate 3-Kinase Catalytic Subunit Delta (*PIK3CD*), C-X-C Motif

Figure 3. FTD3 astrocytes display impaired mitochondrial dynamics

(A) ROS intensity analyzed via fluorescence-activated cell sorting (FACS) and rescue of mitochondrial ROS by treatment with 50 nM UDCA for 24 h.

(B) Mitochondrial function profile.

(C) WB of caspase 3 activity, GAPDH as control.

(D and E) Representative T1A1 labeling and quantification. Scale bar, 25 μm.

(F) Representative mitochondrial distribution. Scale bar, 25 μm.

(G) Running average length of mitochondria.

(H) Qualitative analysis of mitochondria visualized with TEM. Mitochondria are marked by black arrows. Scale bar, 1 μm.

(I) RNA-seq validated by qPCR.

(J and K) qPCR of fission and fusion genes.

(L) Top 20 differentially expressed genes associated with mitochondria. Data are reported as mean ± SEM of three independent experiments. Statistics for RNA-seq, Benjamin-Hochberg adjusted p value (Wald test) $\leq$ 0.05, absolute log2 fold change $\geq$ 1, and mean of normalized counts $\geq$ 10; qPCR, unpaired Student's t test, and other analyses one-way ANOVA with Tukey multiple comparisons test, *p < 0.05, **p < 0.01, and ***p < 0.001. See also Figures S1, S4, Tables S2, and S3.

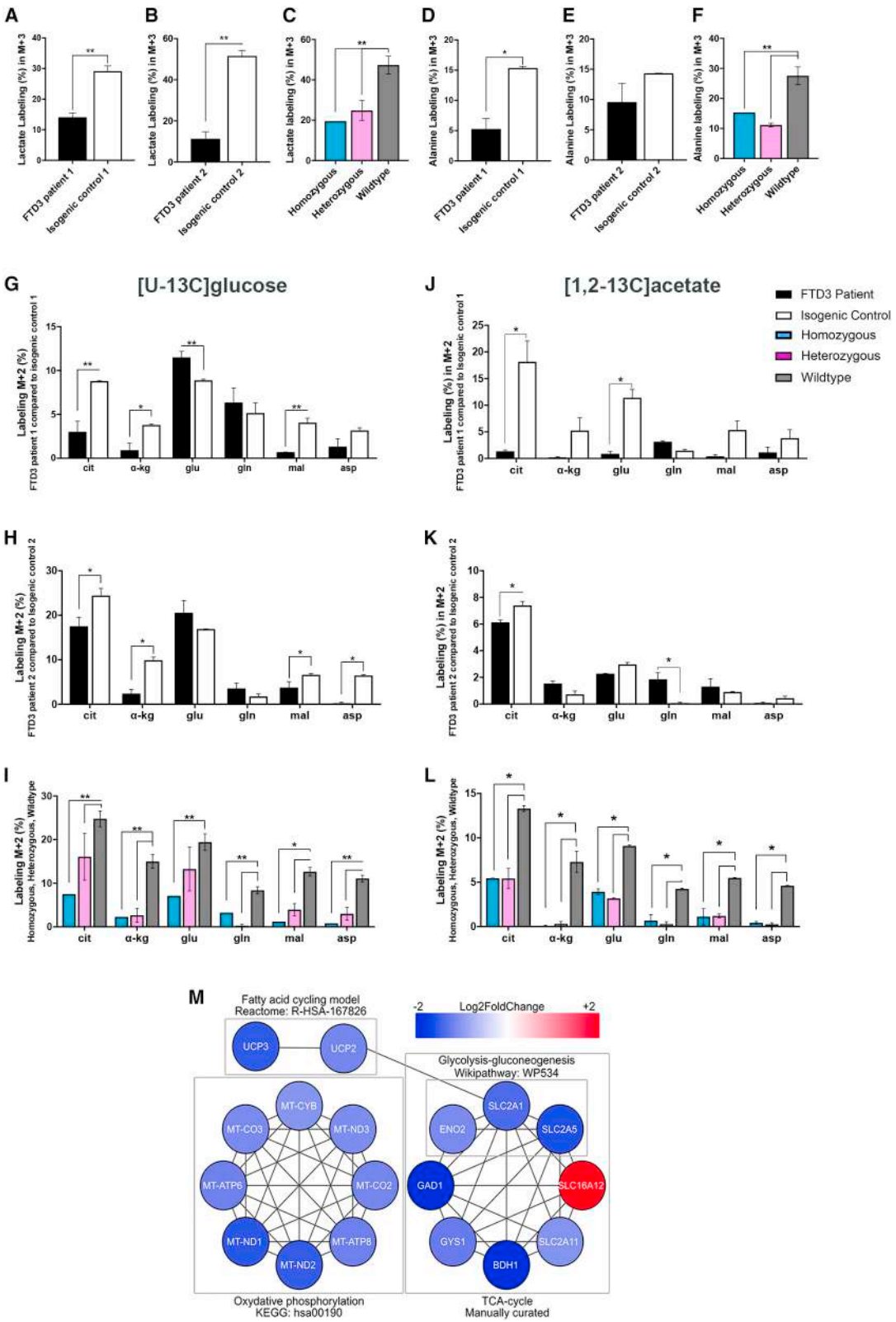

(legend on next page)

Chemokine Ligand 5 (*CXCL5*) and *IL-6*. These data suggest an increased inflammatory response in the FTD3 astrocytes similar to reports in ALS (Chen et al., 2019). Functional and pathway enrichment analysis highlighted cytokine activity and cytokine-cytokine receptor interaction within the most enriched terms (Figures S1C and S1D). Most notably, apolipoprotein D (*APOD*) was found to be upregulated in the FTD3 astrocytes (Table S2). This gene is shown to be upregulated in aging and degenerative brains (Dassati et al., 2014). Furthermore, we observed an upregulation of *IL-17D* (Table S2), a cytokine reported to increase the expression of IL-8 in an NF-κB-dependent manner (Starnes et al., 2002), while Signal Regulatory Protein Alpha (*SIRP-α*), reported as a negative regulator of cytokine production involved in inflammatory response (GO: 1900016) was downregulated. We further observed an upregulation of proteoglycans (PGs) such as biglycan (*BGN*), Syndecan 2 (*SDC2*), aggrecan (*ACAN*), and lumican (*LUM*) (Figure 5P). PGs participate in neuroinflammation and were previously linked to neurodegenerative diseases (Heindryckx and Li, 2018). Of particular interest is the upregulation of *SDC2*, as *SDC2* is known to control a large number of cytokines through proteoglycan-mediated inflammatory responses (Gopal, 2020). In addition, we observed a strong decrease in the expression of the cystic fibrosis transmembrane conductance regulator (*CFTR*) in FTD3 astrocytes (Figure 5P). Mutation in this gene leads to impaired immune cell functions and exaggerated pro-inflammatory responses in AD (Lahousse et al., 2003), while knockdown causes an increase in basal secretion of IL-8 as well as IL-1β-induced secretion of IL-6 and IL-8 (Crites et al., 2015). Collectively, our findings indicate that conversion of resting astrocytes to reactive astrocytes via NF-κB activation leads to increased pro-inflammatory cytokine release, which triggers an autoregulatory loop reinforcing the toxic reactive astrocyte phenotype and further enhances cytokine production.

Reactive astrocyte media inhibit axonal outgrowth

Previous research has demonstrated that secreted factors from reactive astrocytes impair neurite outgrowth (Sofroniew, 2015). To investigate this toxic effect, we cultured healthy neurons with astrocyte conditioned medium (ACM) from FTD3 and control astrocytes. A decrease in neurite length was observed in neurons cultured with FTD3 ACM compared with control ACM (Figures 5Q and 5R), demonstrating the inhibiting impact on neuronal outgrowth via secreted factors from FTD3 astrocytes. Moreover, we analyzed the expression levels of genes associated with the positive and negative regulation of the glial cell apoptotic process (according to GO: 0034352 and GO: 0034351) via RNA-seq analysis. We observe upregulation of A-Kinase Anchoring Protein 12 (*AKAP12*) and downregulation of Growth Arrest Specific 6 (*GAS6*) in FTD3 astrocytes (Table S2). AKAP12 is involved in oligodendrocyte apoptosis and in the production of TNF-α as well as nitric oxide in astrocytes with inflammatory stimulation (Li et al., 2010). GAS6 promotes cell survival in the brain (Axelrod and Pienta, 2014). These results further underline the overall toxic effect of astrocytes in FTD3 patients reflected in the pathology of cortical neurodegeneration.

DISCUSSION

A previous study reports that excess accumulation of autophagosomes has a negative impact on neuronal survival, and dysfunctional ESCRT-III appears to cause neurodegeneration through numerous mechanisms (Lee et al., 2009a). However, the involvement of autophagy in astrocytes is largely unknown. In this study, we report that astrocytes generated from FTD3 patient hiPSCs, or with introduced CHMP2B mutation, display autophagy impairments with autophagosome accumulation. The ICC and WB results, together with the accumulation of cargo-filled vesicles visualized with TEM, are reliable indications that the autophagy process is impaired and that FTD3 astrocytes are unsuccessfully attempting to accommodate the degradation of a large amount of intracellular material. These results were confirmed in the CHMP2B^{intron5} mice model (Krasniak and Ahmad, 2016). Despite the increase in autophagic flux and our attempt to promote autophagic clearance of accumulated autophagosomes with rapamycin, we did not see a reduction in autophagosomes. This suggests that one or several steps in the autophagic process is affected in FTD3 astrocytes. Our investigation of RAB7-mediated transport, which is affected in FTD3 neurons (Urwin et al., 2010), did not show a similar phenotype, and neither did our investigation of the autophagosome-lysosomal fusion; however, this does not exclude the possibility of faulty transport and fusion involvements.

Figure 4. Energy hypometabolism in FTD3 astrocytes

(A–I) Glucose metabolism: 13C enrichment in metabolites was determined via GC-MS after 90-min incubation with [U-13C] glucose

(J–I) Acetate metabolism.

(M) Networks of downregulated genes involved in energy-production pathways. Node colors represent expression fold changes in a blue-white-red logarithmic scale. Mean ± SEM of three independent experiments. Two-way ANOVA with Tukey multiple comparisons test; *$p < 0.05$, **$p < 0.01$. See also Figures S1, S5, Tables S2, and S3.

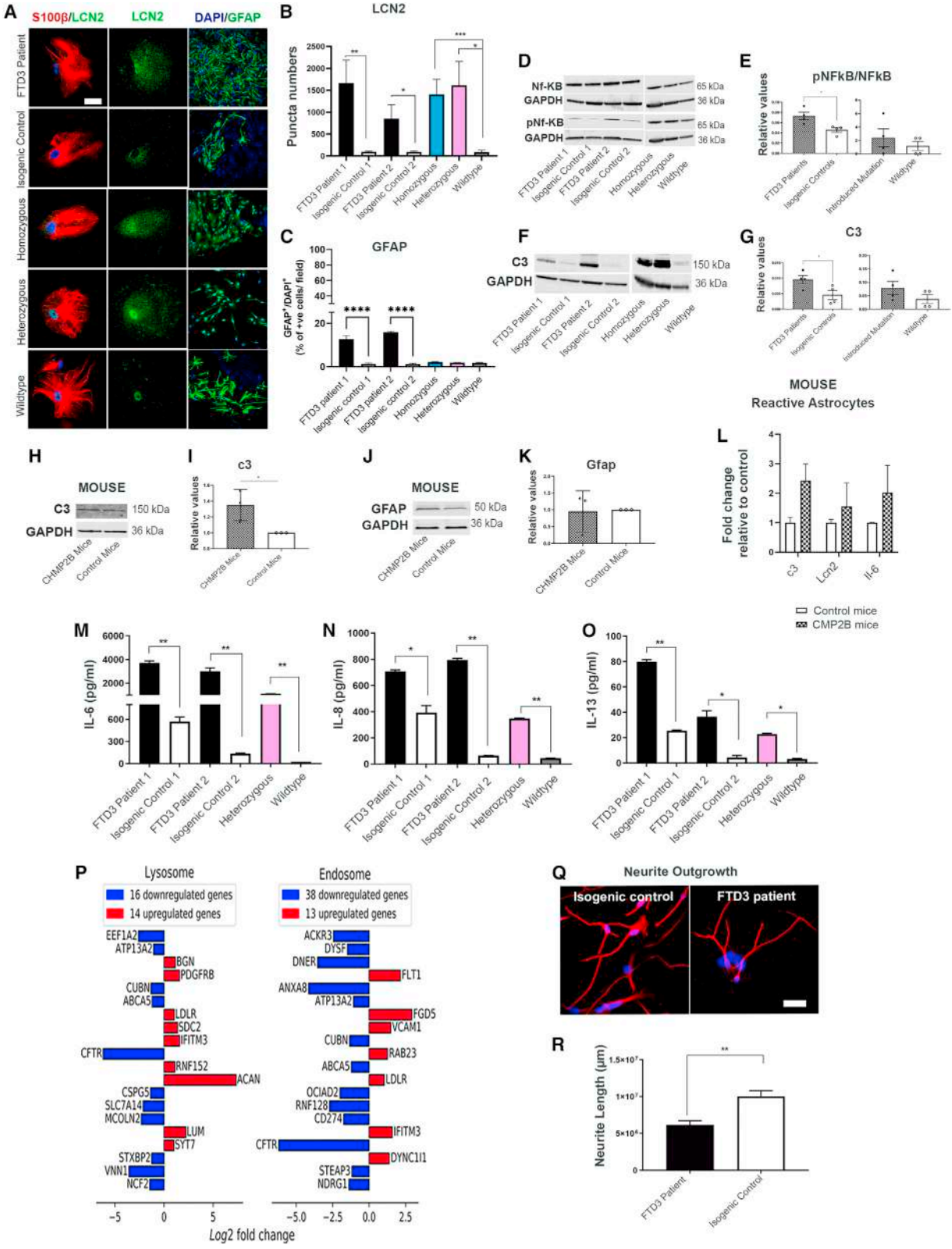

(legend on next page)

Defective recycling of organelles is the earliest impairment event, which clearly links autophagy to mitochondria turnover (Xie et al., 2015). Abnormal mitochondrial function and aberrant morphology were previously reported by our group in hiPSC-derived FTD3 neurons (Zhang et al., 2017). Consistent with this, we here present mitochondrial dysfunctions with hypometabolism, increased mitochondrial fusion, and release of ROS as central components of FTD3 astrocyte pathology. We could indeed rescue mitochondrial ROS levels in FTD3 astrocytes via UDCA; however, we did not see an effect on other mitochondrial phenotypes.

Increased mitochondrial fusion is an important mechanism in metabolically active cells in order to provide a mitochondrial network that can sustain and accommodate the need for large amount of energy (Krasniak and Ahmad, 2016). In quiescent cells, where the energy demand is less, the mitochondria often appear smaller and spherical due to increased fission activity (Westermann, 2010). Since the FTD3 astrocytes demonstrate hypometabolism with decreased glycolysis and TCA cycle activity, we propose an increased fusion of functional and damaged mitochondria as a regulatory mitochondrial attempt to accommodate the energy demand in the cells. This could explain the increased and elongated network of mitochondria evident in the FTD3 astrocytes. The upregulation of the lactate labeling after incubation with [U-^{13}C] glutamate, which supports an increased incorporation of the carbon skeleton of glutamate into lactate possibly via malic enzyme (McKenna et al., 1995), might also be a compensatory mechanism against the hypometabolism.

It has been reported that oxidative stress induces autophagy impairments, driving the accumulation of dysfunctional mitochondria (Luo et al., 2013). Similarly, we showed that oxidative stress causes defects in the autophagy-mitophagy pathway, as it directly connects cellular clearance mechanisms with mitochondrial function. We suggest that autophagy imbalances are causing an accumulation of dysfunctional mitochondria further prompting the hypometabolism (graphical abstract).

A subtype of reactive astrocytes can be toxic to neurons by promoting the loss of beneficial astrocytic properties such as neural outgrowth and synaptogenesis, thereby resulting in neuronal cell death (Escartin et al., 2021). In the toxic subtype of reactive astrocytes, our study reveals that FTD3 astrocytes upregulate characteristic genes such as *SERPING1* and *FBLN5*. Astrocyte expressing SERPING1 may lead to recruitment of large numbers of T lymphocytes, exacerbating neuroinflammation via complement cascade in the brain (Hennessy et al., 2015). Glial cell reactivity is increasingly connected to neurodegenerative diseases (Liddelow and Barres, 2017); especially in AD, an upregulation of astrocytic pro-inflammatory cytokines such as TNFα and IL-1β has been shown to cause astrocyte reactivity (Oksanen et al., 2017). Likewise in ALS, increased levels of TGF-β1, produced by SOD1 G93A reactive astrocytes, induces cytoplasmic aggregation and impaired autophagy (Tripathi et al., 2017). Here, we showed that mutations in CHMP2B causing FTD3 contribute to astrocyte reactivity by upregulation of LCN2 and GFAP. Supporting our findings, studies suggest that increased levels of LCN2 were detected in the cerebrospinal fluid of patients with AD and in the frontal cortex of patients with FTLD, correlating with reactive astrocyte pathology (Bi et al., 2013). In accordance, we observed an increase in the pro-inflammatory cytokine secretion from FTD3 astrocytes. The results are consistent with previous findings where increases in IL-6 and IL-8 in the brain tissues were associated with poor cognitive performance (Jabbari Azad et al., 2014). It should be noted that these cytokines, when secreted by activated microglia, could induce the formation of reactive astrocytes (Cregg et al., 2014); However, due to the absence of microglia in our cultures, we hypothesize that an autoregulatory cytokine loop drives the reactive astrocytes phenotype in FTD3 astrocytes through NF-κB activation. Finally, we investigated the presence of astrocyte reactivity in CHMP2B^{intron5}mice brains, where our findings

Figure 5. FTD3 pathology contributes to reactive astrocyte

(A) Representative images of LCN2 and S100 β co-labeling of astrocytes (left column) and GFAP labeling of astrocytes (right column). Scale bar, 25 μm.
(B) LCN2 puncta quantification.
(C) GFAP quantification.
(D and E) WB of NF-κB and phosphorylated-NF-κB (pNF-κB).
(F and G) WB of C3 (human).
(H and I) WB of C3 for CHMP2B^{intron5} mice brain.
(J and K) WB of GFAP (mouse).
(L) Validation of CHMP2B^{intron5} mice brain for reactive astrocytes.
(M–O) Cytokine profiling.
(P) Top 20 differentially expressed genes associated with lysosomes (left) and endosomes (right).
(Q) Representative image of neurite outgrowth.
(R) Neurite outgrowth quantification. Mean ± SEM of three independent experiments. One-way ANOVA with Tukey multiple comparisons test; *p < 0.05, **p < 0.01, ***p < 0.001, and ****p < 0.0001. See also Figures S1, S5, Tables S2, and S3.

revealed complement protein C3 as an astroglial target of NFκB to be upregulated (Lian et al., 2015).

In summary, our findings show that FTD3 astrocytes have perturbed autophagy with accumulation of amphisomes. This autophagy impairment leads to insufficient mitochondrial turnover with increased fusion and elongated mitochondrial morphology. This kind of mitochondrial fusion mechanism is needed to accommodate the energy demands. Eventually, this continued dysfunction in combination with an increase in ROS results in metabolic failure causing the profound hypometabolism found in FTD3 astrocytes. These cascades of events ultimately cause a shift in astrocyte homeostasis resulting in a switch to a reactive astrocyte phenotype with subsequent increased release of neurotoxic cytokines, leading to NF-κB pathway activation with increased production of GFAP, LCN2, and C3. Finally, we were able to validate the reactive astrocyte phenotype both *in vivo* and *in vitro*. Our data provide mechanistic insights into how defective autophagy causes altered mitochondrial dynamics, leading to the adoption of reactive astrocyte properties with increased cytokine release, NF-κB activation, and expression of neurotoxic proteins, indicating how astrocytes contribute to neurodegeneration in FTD3.

EXPERIMENTAL PROCEDURES

See supplemental information for detailed descriptions of the methods.

Cell culture, iPSC generation, and astrocyte differentiation

All hiPSC lines used in this study were characterized and published earlier in Rasmussen et al. (2014) and Zhang et al. (2017). Astrocytes differentiation followed a modified protocol (Shaltouki et al., 2013).

WB, ICC, TEM, and qPCR

WB, ICC, TEM, and qPCR methods are described in the supplemental information. See also Table S4.

Metabolomics

Cell extracts were lyophilized and reconstituted in water for Pierce BCA assay and metabolites were mapped using a gas chromatograph (Agilent Technologies 7820A chromatograph, J&W GC column HP-5MS, part no. 19091S-433) coupled to a mass spectrometer (Agilent Technologies, 5977E). Data are presented as labeling (%) of M + X, where M is the mass of the unlabeled molecule and X is the number of labeled C atoms in a given metabolite.

Multiplex array

Cytokine measurements were made using the Meso Scale Discovery, K15067L-1. The commercial human-specific U-PLEX Biomarker Group 1 was used. Samples were measured according to manufactures protocol.

Statistical analysis

For all experiments, data are presented as mean ± standard errors of the mean (SEM) of three independent experiments. Statistical analysis were made in GraphPad Prism 7.03. Statistical analyses were determined using Student's t test or by one-way ANOVA with a Tukey's post test or by two-way ANOVA with Bonferroni post hoc test for differences of mean between each groups. Statistical significance are labeled in the figures as *p < 0.05, **p < 0.01, ***p < 0.001, ****p < 0.0001.

Data and code availability

The datasets used and analyzed during this study are available in the source data file. The dataset generated for RNA-seq has been deposited in the NCBI GEO database under the accession number GEO: GSE141388.

SUPPLEMENTAL INFORMATION

Supplemental information can be found online at https://doi.org/10.1016/j.stemcr.2021.09.013.

AUTHOR CONTRIBUTIONS

A.C. and K.K.F. performed experimental design. A.C. generated hiPSC-derived astrocytes. A.C. and K.S.D performed most of the experiments. B.I.A. and C.A. performed metabolic profiling. A.C., K.S.D., and K.K.F. interpreted the results and wrote the manuscript. G.I.C. and N.T.D. analyzed RNA-seq data and made gene network analysis under supervision of J.G. A.C. and S.A. were involved in the analyses of RNA-seq data. S.C. helped in data analysis of the qPCR experiment. M.P. prepared samples for TEM. H.H. analyzed TEM samples. S.I.S. and M.M. performed cytokine assays. J.K., P.H., and A.D. edited and approved the paper. All authors read and approved the final version of the paper.

CONFLICTS OF INTEREST

The authors declare no competing interests.

ACKNOWLEDGMENTS

We are grateful to Dr. Adrian M. Isaacs for providing CHMP2B^{intron5} and control mouse brain samples. The authors are grateful to Philip Seymour for proof reading the paper. We thank Amelia M Hall for her help with TEM analysis. This work was supported by awards from Independent Research Fund Denmark (FTP, grant no. 109799) (K.K.F.), Innovation Fund Denmark (BrainStem, 4108-00008B and NeuroStem, 4096-00001B) (K.K.F.), Alzheimer Foundation Denmark (K.K.F.), Novo Nordisk Foundation (GliAD—NNF18OC0052369 and NNF19OC0058399) (K.K.F.). A.D. was supported by EUH2020 JPCO-Fund call for Personalized Medicine JPND2019-466-037/2019-2.1.7-ERA-NET-2020-00007 (ADAIR).

Received: March 30, 2021
Revised: September 20, 2021
Accepted: September 21, 2021
Published: October 21, 2021

REFERENCES

Aldana, B.I., Zhang, Y., Jensen, P., Chandrasekaran, A., Christensen, S.K., Nielsen, T.T., Nielsen, J.E., Hyttel, P., Larsen, M.R., Waagepetersen, H.S., et al. (2020). Glutamate-glutamine homeostasis is perturbed in neurons and astrocytes derived from patient iPSC models of frontotemporal dementia. Mol. Brain *13*, 1–17.

Autret, A., and Martin, S.J. (2010). Bcl-2 family proteins and mitochondrial fission/fusion dynamics. Cell. Mol. Life Sci. *67*, 1599–1606.

Axelrod, H., and Pienta, K.J. (2014). Axl as a mediator of cellular growth and survival. Oncotarget *5*, 8818–8852.

Azevedo, F.A.C., Carvalho, L.R.B., Grinberg, L.T., Farfel, J.M., Ferretti, R.E.L., Leite, R.E.P., Filho, W.J., Lent, R., and Herculano-Houzel, S. (2009). Equal numbers of neuronal and nonneuronal cells make the human brain an isometrically scaled-up primate brain. J. Comp. Neurol. *513*, 532–541.

Bi, F., Huang, C., Tong, J., Qiu, G., Huang, B., Wu, Q., Li, F., Xu, Z., Bowser, R., Xia, X.G., et al. (2013). Reactive astrocytes secrete lcn2 to promote neuron death. Proc. Natl. Acad. Sci. U S A *110*, 4069–4074.

Chen, Y., Xia, K., Chen, L., and Fan, D. (2019). Increased interleukin-6 levels in the astrocyte-derived exosomes of sporadic amyotrophic lateral sclerosis patients. Front. Neurosci. *13*, 574.

Cregg, J.M., DePaul, M.A., Filous, A.R., Lang, B.T., Tran, A., and Silver, J. (2014). Functional regeneration beyond the glial scar. Exp. Neurol. *253*, 197–207.

Crites, K.S.M., Morin, G., Orlando, V., Patey, N., Cantin, C., Martel, J., Brochiero, E., and Mailhot, G. (2015). CFTR Knockdown induces proinflammatory changes in intestinal epithelial cells. J. Inflamm. *12*, 62.

Danbolt, N.C. (2001). Glutamate uptake. Prog. Neurobiol. *65*, 1–105.

Dassati, S., Waldner, A., and Schweigreiter, R. (2014). Apolipoprotein D takes center stage in the stress response of the aging and degenerative brain. Neurobiol. Aging *35*, 1632–1642.

Ding, W.X., and Yin, X.M. (2012). Mitophagy: mechanisms, pathophysiological roles, and analysis. Biol. Chem. *393*, 547–564.

Edens, B.M., Miller, N., and Ma, Y.C. (2016). Impaired autophagy and defective mitochondrial function: converging paths on the road to motor neuron degeneration. Front. Cell. Neurosci. *10*, 44.

Escartin, C., Galea, E., Lakatos, A., O'Callaghan, J.P., Petzold, G.C., Serrano-Pozo, A., Steinhäuser, C., Volterra, A., Carmignoto, G., Agarwal, A., et al. (2021). Reactive astrocyte nomenclature, definitions, and future directions. Nat. Neurosci. *24*, 312.

Fonseca, T.B., Sánchez-Guerrero, Á., Milosevic, I., and Raimundo, N. (2019). Mitochondrial fission requires DRP1 but not dynamins. Nature *570*, E34–E42.

Fraczek, L.A., Martin, C.B., and Martin, B.K. (2011). c-Jun and c-Fos regulate the complement factor H promoter in murine astrocytes. Mol. Immunol. *49*, 201–210.

Gopal, S. (2020). Syndecans in inflammation at a glance. Front. Immunol. *11*, 1–5.

Haim, L.B., Carrillo-de Sauvage, M.A., Ceyzériat, K., and Escartin, C. (2015). Elusive roles for reactive astrocytes in neurodegenerative diseases. Front. Cell. Neurosci. *9*, 278.

Heindryckx, F., and Li, J.P. (2018). Role of proteoglycans in neuroinflammation and central nervous system fibrosis. Matrix Biol. *68–69*, 589–601.

Heneka, M.T., Carson, M.J., El Khoury, J., Landreth, G.E., Brosseron, F., Feinstein, D.L., Jacobs, A.H., Wyss-Coray, T., Vitorica, J., Ransohoff, R.M., et al. (2015). Neuroinflammation in Alzheimer's disease. Lancet Neurol. *14*, 388–405.

Hennessy, E., Griffin, E.W., and Cunningham, C. (2015). Astrocytes are primed by chronic neurodegeneration to produce exaggerated chemokine and cell infiltration responses to acute stimulation with the cytokines IL-1β and TNF-α. J. Neurosci. *35*, 8411–8422.

Holzerova, E., Danhauser, K., Haack, T.B., Kremer, L.S., Melcher, M., Ingold, I., Kobayashi, S., Terrile, C., Wolf, P., Schaper, J., et al. (2016). Human thioredoxin 2 deficiency impairs mitochondrial redox homeostasis and causes early-onset neurodegeneration. Brain *139*, 346–354.

Jabbari Azad, F., Talaei, A., Rafatpanah, H., Yousefzadeh, H., Jafari, R., Talaei, A., and Farid Hosseini, R. (2014). Association between cytokine production and disease severity in Alzheimer's disease. Iran. J. Allergy Asthma. Immunol. *13*, 433–439.

Jäger, S., Bucci, C., Tanida, I., Ueno, T., Kominami, E., Saftig, P., and Eskelinen, E.L. (2004). Role for Rab7 in maturation of late autophagic vacuoles. J. Cell Sci. *117*, 4837–4848.

Krasniak, C.S., and Ahmad, S.T. (2016). The role of CHMP2BIntron5 in autophagy and frontotemporal dementia. Brain Res. *1649*, 151–157.

Lahousse, S.A., Stopa, E.G., Mulberg, A.E., and De La Monte, S.M. (2003). Reduced expression of the cystic fibrosis transmembrane conductance regulator gene in the hypothalamus of patients with Alzheimer's disease. J. Alzheimer's Dis. *5*, 455–462.

Lee, F.S., Peters, R.T., Dang, L.C., and Maniatis, T. (1998). MEKK1 activates both IκB kinase α and IκB kinase β. Proc. Natl. Acad. Sci. U S A *95*, 9319–9324.

Lee, J.A., Beigneux, A., Ahmad, S.T., Young, S.G., and Gao, F.B. (2007). ESCRT-III dysfunction causes autophagosome accumulation and neurodegeneration. Curr. Biol. *17*, 1561–1567.

Lee, J.A., Liu, L., and Gao, F.B. (2009a). Autophagy defects contribute to neurodegeneration induced by dysfunctional ESCRT-III. Autophagy *5*, 1070–1072.

Lee, S., Park, J.Y., Lee, W.H., Kim, H., Park, H.C., Mori, K., and Suk, K. (2009b). Lipocalin-2 is an autocrine mediator of reactive astrocytosis. J. Neurosci. *29*, 234–249.

Li, X., Yan, M., Hu, L., Sun, L., Zhang, F., Ji, H., Jiang, J., Wang, P., Liu, H., Gao, Y., et al. (2010). Involvement of Src-suppressed C kinase substrate in experimental autoimmune encephalomyelitis: a link between release of astrocyte proinflammatory factor and oligodendrocyte apoptosis. J. Neurosci. Res. *88*, 1858–1871.

Lian, H., Yang, L., Cole, A., Sun, L., Chiang, A.C.A., Fowler, S.W., Shim, D.J., Rodriguez-Rivera, J., Taglialatela, G., Jankowsky, J.L., et al. (2015). Nfκb-activated astroglial release of complement C3

compromises neuronal morphology and function associated with Alzheimer's disease. Neuron *85*, 101–115.

Liddelow, S.A., and Barres, B.A. (2017). Reactive astrocytes: production, function, and therapeutic potential. Immunity *46*, 957–967.

Liddelow, S.A., Guttenplan, K.A., Clarke, L.E., Bennett, F.C., Bohlen, C.J., Schirmer, L., Bennett, M.L., Münch, A.E., Chung, W.S., Peterson, T.C., et al. (2017). Neurotoxic reactive astrocytes are induced by activated microglia. Nature *541*, 481–487.

Lindquist, S.G., Braendgaard, H., Svenstrup, K., Isaacs, A.M., and Nielsen, J.E. (2008). Frontotemporal dementia linked to chromosome 3 (FTD-3) - current concepts and the detection of a previously unknown branch of the Danish FTD-3 family. Eur. J. Neurol. *15*, 667–670.

Lu, J., and Holmgren, A. (2012). Thioredoxin system in cell death progression. Antioxid. Redox Signal. *17*, 1738–1747.

Luo, C., Li, Y., Wang, H., Feng, Z., Li, Y., Long, J., and Liu, J. (2013). Mitochondrial accumulation under oxidative stress is due to defects in autophagy. J. Cell. Biochem. *114*, 212–219.

McKenna, M.C., Tildon, J.T., Stevenson, J.H., Huang, X., and Kingwell, K.G. (1995). Regulation of mitochondrial and cytosolic malic enzymes from cultured rat brain astrocytes. Neurochem. Res. *20*, 1491–1501.

McKenna, M.C., Dienel, G.A., Sonnewald, U., Waagepetersen, H.S., and Schousboe, A. (2012). Energy metabolism of the brain. In Basic Neurochemistry (Elsevier), pp. 200–231.

Mortiboys, H., Aasly, J., and Bandmann, O. (2013). Ursocholanic acid rescues mitochondrial function in common forms of familial Parkinson's disease. Brain *136*, 3038–3050.

Nakamura, S., and Yoshimori, T. (2017). New insights into autophagosome-lysosome fusion. J. Cell Sci. *130*, 1209–1216.

Oksanen, M., Petersen, A.J., Naumenko, N., Puttonen, K., Lehtonen, Š., Gubert Olivé, M., Shakirzyanova, A., Leskelä, S., Sarajärvi, T., Viitanen, M., et al. (2017). PSEN1 mutant iPSC-derived model reveals severe astrocyte pathology in Alzheimer's disease. Stem Cell Reports *9*, 1885–1897.

Osborn, L.M., Kamphuis, W., Wadman, W.J., and Hol, E.M. (2016). Astrogliosis: an integral player in the pathogenesis of Alzheimer's disease. Prog. Neurobiol. *144*, 121–141.

Pugsley, H.R. (2017). Assessing autophagic flux by measuring LC3, p62, and LAMP1 co-localization using multispectral imaging flow cytometry. J. Vis. Exp. *1*, 55637.

Qian, K., Huang, H., Peterson, A., Hu, B., Maragakis, N.J., Ming, G.L., Chen, H., and Zhang, S.C. (2017). Sporadic ALS astrocytes induce neuronal degeneration in vivo. Stem Cell Reports *8*, 843–855.

Radford, R.A., Morsch, M., Rayner, S.L., Cole, N.J., Pountney, D.L., and Chung, R.S. (2015). The established and emerging roles of astrocytes and microglia in amyotrophic lateral sclerosis and frontotemporal dementia. Front. Cell. Neurosci. *9*, 27.

Rasmussen, M.A., Holst, B., Tümer, Z., Johnsen, M.G., Zhou, S., Stummann, T.C., Hyttel, P., and Clausen, C. (2014). Transient p53 suppression increases reprogramming of human fibroblasts without affecting apoptosis and DNA damage. Stem Cell Rep. *3*, 404–413.

Rea, S.L., Majcher, V., Searle, M.S., and Layfield, R. (2014). SQSTM1 mutations - bridging Paget disease of bone and ALS/FTLD. Exp. Cell Res. *325*, 27–37.

Shaltouki, A., Peng, J., Liu, Q., Rao, M.S., and Zeng, X. (2013). Efficient generation of astrocytes from human pluripotent stem cells in defined conditions. Stem Cells *31*, 941–952.

Silva, J.M., Rodrigues, S., Sampaio-Marques, B., Gomes, P., Neves-Carvalho, A., Dioli, C., Soares-Cunha, C., Mazuik, B.F., Takashima, A., Ludovico, P., et al. (2019). Dysregulation of autophagy and stress granule-related proteins in stress-driven Tau pathology. Cell Death Differ. *26*, 1411–1427.

Skibinski, G., Parkinson, N.J., Brown, J.M., Chakrabarti, L., Lloyd, S.L., Hummerich, H., Nielsen, J.E., Hodges, J.R., Spillantini, M.G., Thusgaard, T., et al. (2005). Mutations in the endosomal ESCRTIII-complex subunit CHMP2B in frontotemporal dementia. Nat. Genet. *37*, 806–808.

Sofroniew, M.V. (2015). Astrocyte barriers to neurotoxic inflammation. Nat. Rev. Neurosci. *16*, 249–263.

Starnes, T., Broxmeyer, H.E., Robertson, M.J., and Hromas, R. (2002). Cutting edge: IL-17D, a novel member of the IL-17 family, stimulates cytokine production and inhibits hemopoiesis. J. Immunol. *169*, 642–646.

Tripathi, P., Rodriguez-Muela, N., Klim, J.R., de Boer, A.S., Agrawal, S., Sandoe, J., Lopes, C.S., Ogliari, K.S., Williams, L.A., Shear, M., et al. (2017). Reactive astrocytes promote ALS-like degeneration and intracellular protein aggregation in human motor neurons by disrupting autophagy through TGF-β1. Stem Cell Reports *9*, 667–680.

Urwin, H., Authier, A., Nielsen, J.E., Metcalf, D., Powell, C., Froud, K., Malcolm, D.S., Holm, I., Johannsen, P., Brown, J., et al. (2010). Disruption of endocytic trafficking in frontotemporal dementia with CHMP2B mutations. Hum. Mol. Genet. *19*, 2228–2238.

West, R.J.H., Ugbode, C., Fort-Aznar, L., and Sweeney, S.T. (2020). Neuroprotective activity of ursodeoxycholic acid in CHMP2BIntron5 models of frontotemporal dementia. Neurobiol. Dis. *144*, 105047.

Westermann, B. (2010). Mitochondrial fusion and fission in cell life and death. Nat. Rev. Mol. Cell Biol. *11*, 872–884.

Xia, Y., Wu, Z., Su, B., Murray, B., and Karin, M. (1998). JNKK1 organizes a MAP kinase module through specific and sequential interactions with upstream and downstream components mediated by its amino- terminal extension. Genes Dev. *12*, 3369–3381.

Xie, Y., Zhou, B., Lin, M.Y., Wang, S., Foust, K.D., and Sheng, Z.H. (2015). Endolysosomal deficits augment mitochondria pathology in spinal motor neurons of asymptomatic fALS mice. Neuron *87*, 355–370.

Yoon, Y., Krueger, E.W., Oswald, B.J., and McNiven, M.A. (2003). The mitochondrial protein hFis1 regulates mitochondrial fission in mammalian cells through an interaction with the dynamin-like protein DLP1. Mol. Cell. Biol. *23*, 5409–5420.

Yu, R., Lendahl, U., Nistér, M., and Zhao, J. (2020). Regulation of mammalian mitochondrial dynamics: opportunities and challenges. Front. Endocrinol. (Lausanne). *11*, 374.

Zhang, X., Ge, Y.-L., Zhang, S.-P., Yan, P., and Tian, R.-H. (2014). Downregulation of KDR expression induces apoptosis in breast cancer cells. Cell. Mol. Biol. Lett. *19*, 527–541.

Zhang, Y., Schmid, B., Nikolaisen, N.K., Rasmussen, M.A., Aldana, B.I., Agger, M., Calloe, K., Stummann, T.C., Larsen, H.M., Nielsen, T.T., et al. (2017). Patient iPSC-derived neurons for disease modeling of frontotemporal dementia with mutation in CHMP2B. Stem Cell Reports *8*, 648–658.

Zhao, D., Hong, D., Zhang, W., Yao, S., Qi, X., Lv, H., Zheng, R., Feng, L., Huang, Y., Yuan, Y., et al. (2011). Mutations in mitochondrially encoded complex i enzyme as the second common cause in a cohort of Chinese patients with mitochondrial myopathy, encephalopathy, lactic acidosis and stroke-like episodes. J. Hum. Genet. *56*, 759–764.

Stem Cell Reports, Volume *16*

Supplemental Information

Astrocytic reactivity triggered by defective autophagy and metabolic failure causes neurotoxicity in frontotemporal dementia type 3

Abinaya Chandrasekaran, Katarina Stoklund Dittlau, Giulia I. Corsi, Henriette Haukedal, Nadezhda T. Doncheva, Sarayu Ramakrishna, Sheetal Ambardar, Claudia Salcedo, Sissel I. Schmidt, Yu Zhang, Susanna Cirera, Maria Pihl, Benjamin Schmid, Troels Tolstrup Nielsen, Jørgen E. Nielsen, Miriam Kolko, Julianna Kobolák, András Dinnyés, Poul Hyttel, Dasaradhi Palakodeti, Jan Gorodkin, Ravi S. Muddashetty, Morten Meyer, Blanca I. Aldana, and Kristine K. Freude

Supplemental Information

Supplemental table of contents

Supplemental Figures

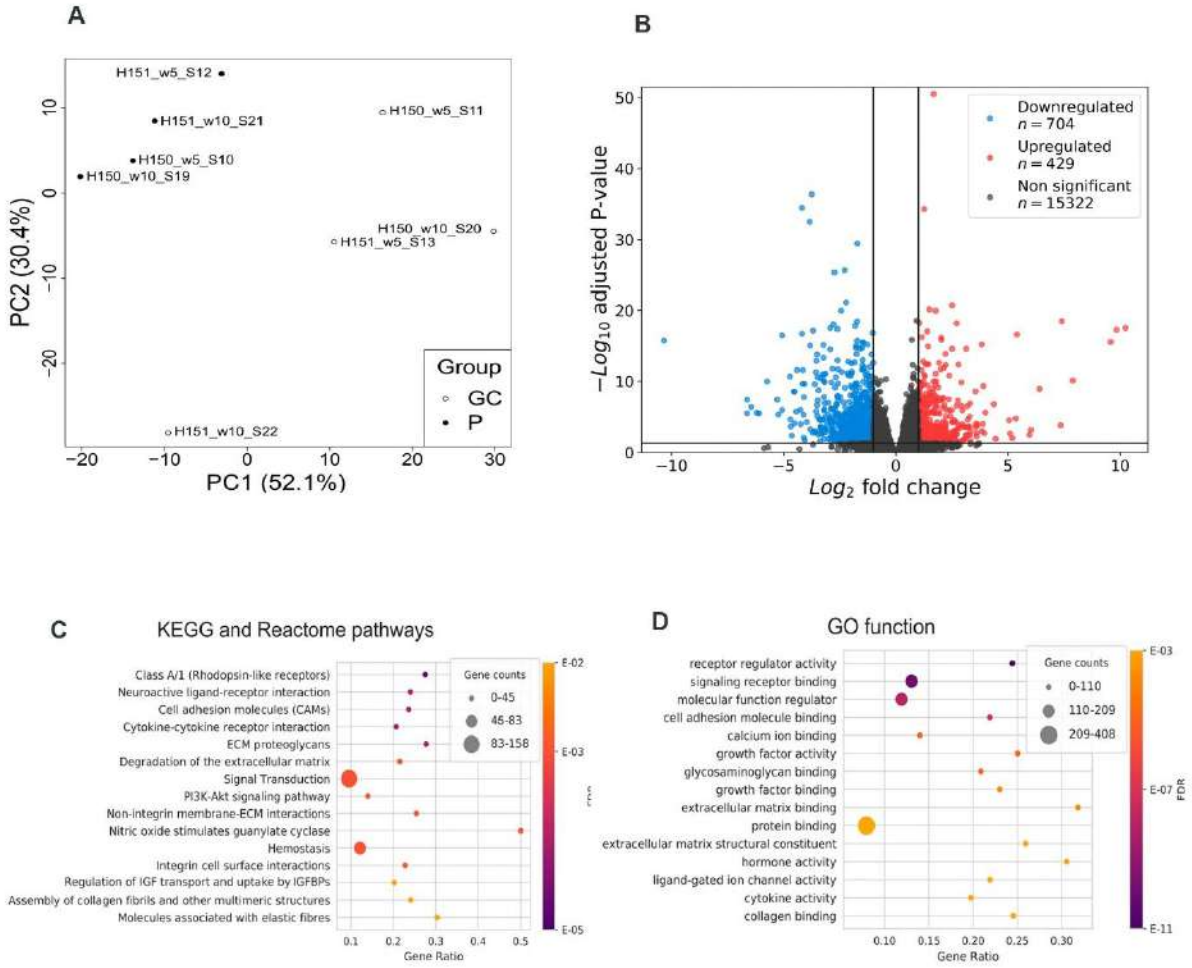

Figure S1. Transcriptome analysis. Related to Figure 3-5.
Expression-based Principal Component (PC) analysis shows consistent separation between FTD3 patient astrocytes and isogenic controls. The results consistently separated FTD3 patient lines and control lines based on their gene expression levels via PC analysis. **B)** Volcano plot of genes with a mean of DESeq2-normalized counts >= 10 differentially expressed between FTD3 patient astrocytes and isogenic controls. Genes with absolute log2FoldChange >= 1 and adjusted p-value <= 0.05 are selected as significantly differentially expressed and colored in blue or red if down- or upregulated, respectively. Analysis of differential gene expression between patient and control astrocytes, revealed 1,133 genes with a log2 fold change (LFC) of gene expression ≥ 1; and a significant P-value (<=0.05) after adjusting for multiple testing **C)** Top 15 significantly enriched KEGG and Reactome pathways identified by functional enrichment analysis of all 1133 significantly differentially expressed genes between FTD3 patient astrocytes and isogenic controls. The gene ratio corresponds to the ratio between the differentially expressed and all expressed genes annotated with a term. For each enriched term, the size of the dot indicates the number of differentially expressed genes annotated with this term, while the color shows the FDR of the enrichment test. **D**) The same representation as in (c) is used for the top 15 significantly enriched Gene Ontology (GO) functions.

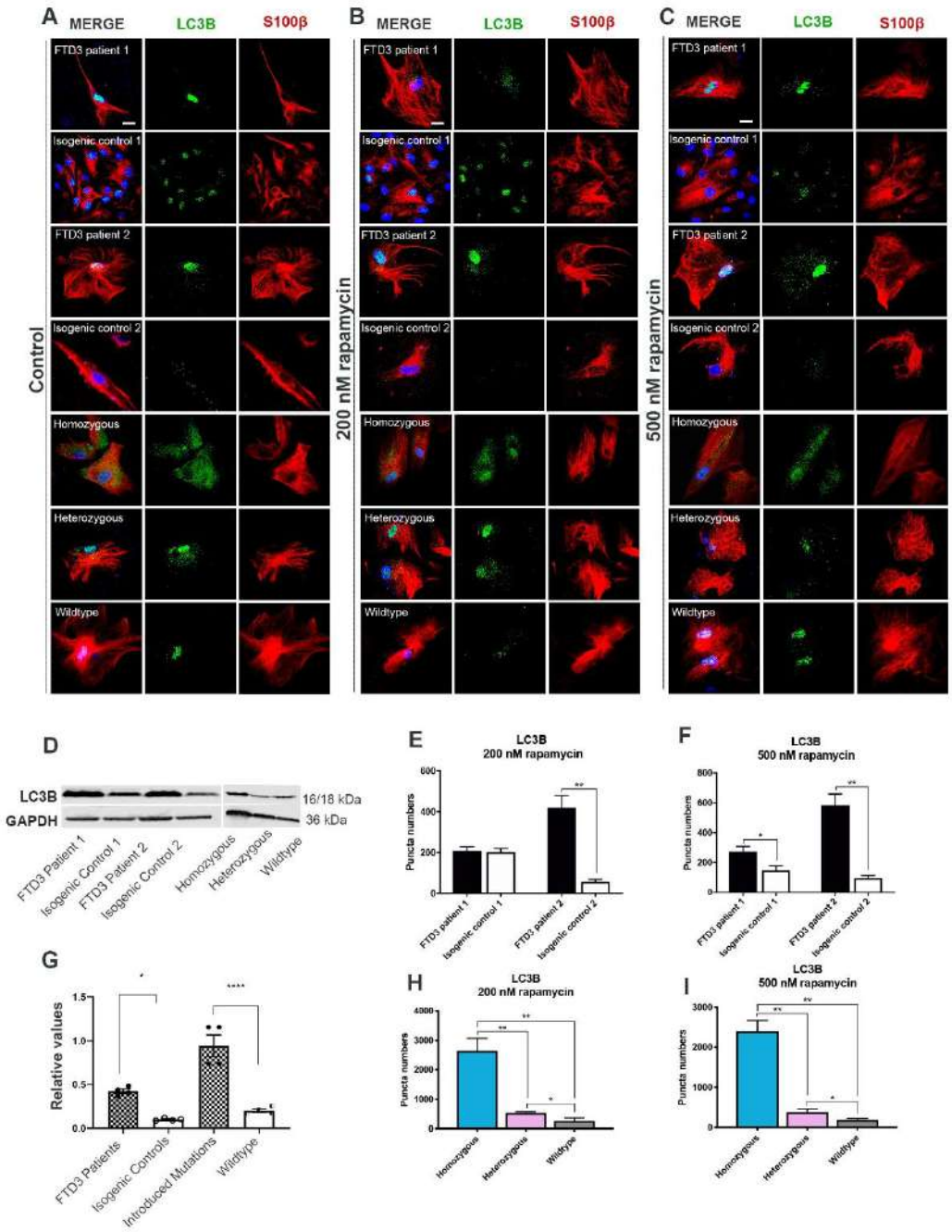

Figure S2. Characterization of autophagy at different rapamycin treatment concentrations. Related to Figure 2.

A-C) Representative ICC images of LC3B and S100β co-labelling of astrocytes at 0nM, 200nM and 500nM rapamycin treatment. LC3B is a marker of autophagosomes. S100B is utilized as a cytoplasmic marker to visualize LC3B intracellular distribution. Scale bar, 25 µm. **D+G)** WB analysis of LC3B. Data represented as mean ± SEM. One-way ANOVA with Tukey multiple comparisons test; *p<0.05 and ****p <0.0001. **E-F+H-I)** LC3B puncta number quantification of astrocytes at different rapamycin concentrations. Data represented as mean ± SEM of three independent experiments. One-way ANOVA with Tukey multiple comparisons test; *p<0.05 and **p <0.01.

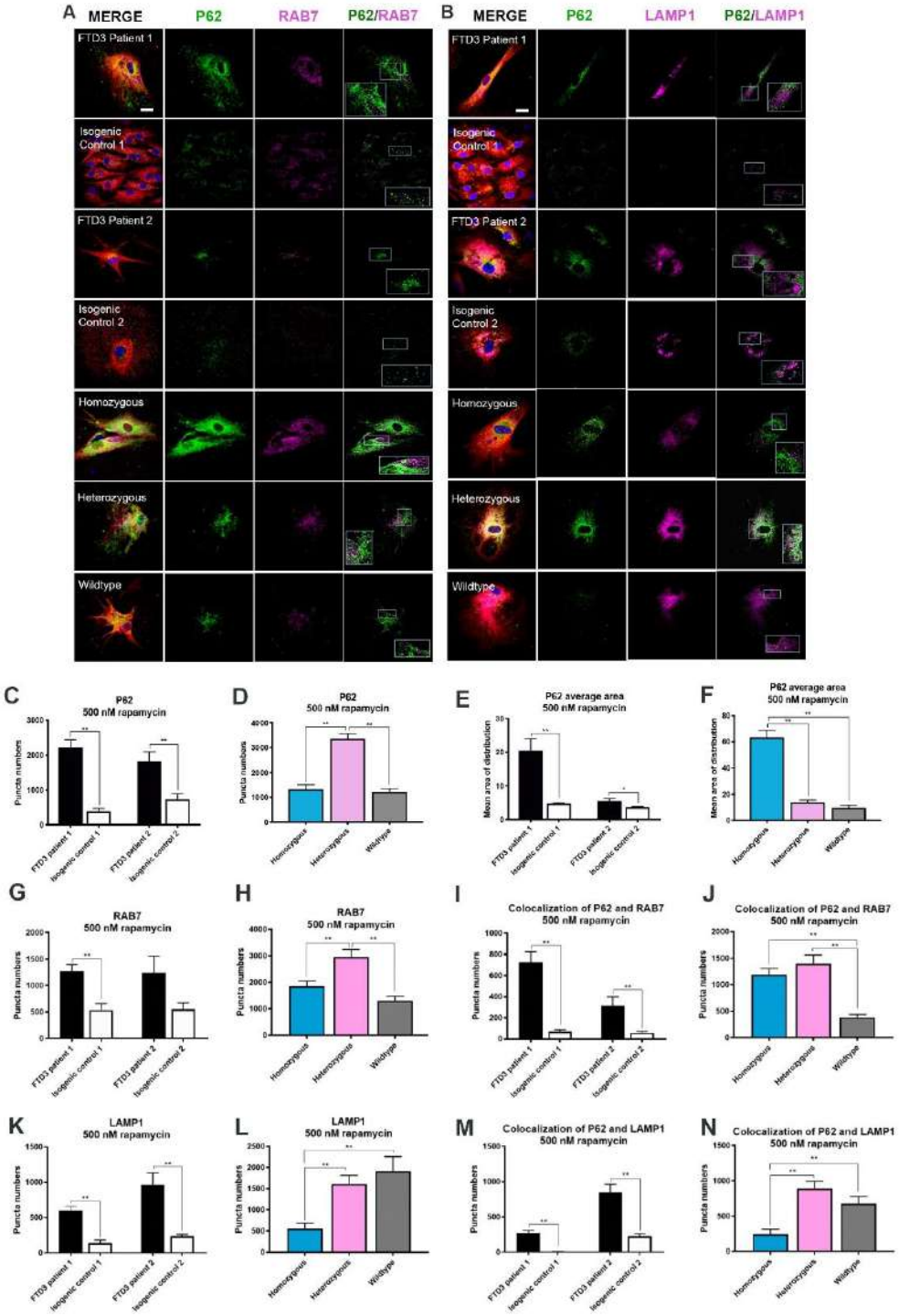

Figure S3. Characterization of autophagy changes with 500 nM rapamycin treatment. **Related to Figure 2.**

A-B) Representative ICC images of P62, AQP4 and RAB7 (**A**) and P62, AQP4 and LAMP1 (**B**) co-labelling of astrocytes with 500 nM rapamycin treatment. Scale bar, 25 µm. **C-J)** ICC quantifications of P62, RAB7, and P62 mean area and co-localization puncta number of FTD3 patient, heterozygous, homozygous astrocytes vs controls. Data represented as mean ± SEM of three independent experiments. One-way ANOVA with Tukey multiple comparisons test; *p<0.05 and **p <0.01. **K-N)** LAMP1 and co-localization puncta number quantification of FTD3 astrocytes and controls with 500 nM rapamycin treatment. Data

represented as mean ± SEM. One-way ANOVA with Tukey multiple comparisons test; *p<0.05, **p <0.01 and ***p <0.001.

Figure S4

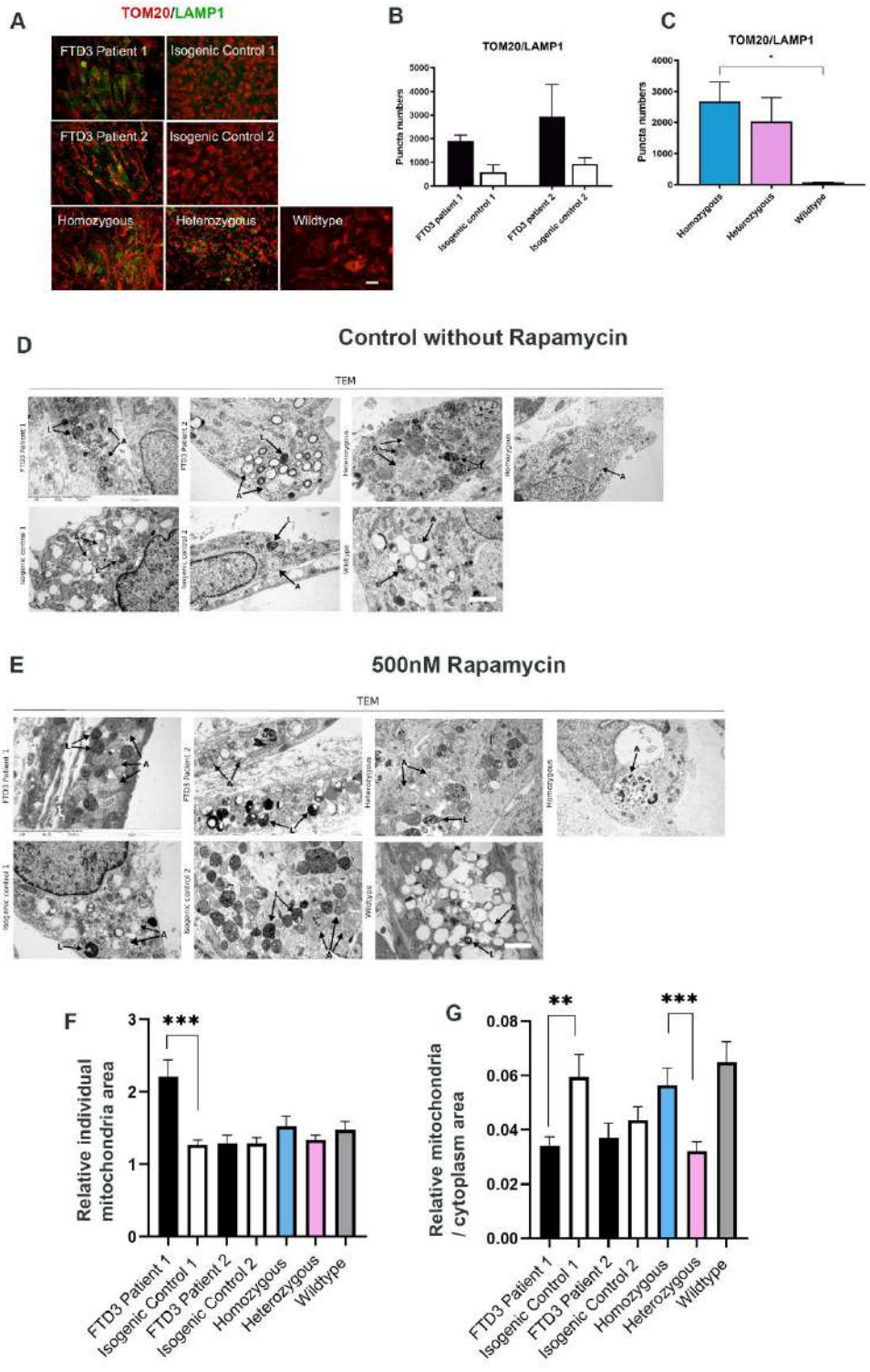
A
TOM20/LAMP1
FTD3 Patient 1
Isogenic Control 1
FTD3 Patient 2
Isogenic Control 2
Homozygous
Heterozygous
Wildtype
B
TOM20/LAMP1
Puncta numbers
FTD3 patient 1
Isogenic control 1
FTD3 patient 2
Isogenic control 2
C
TOM20/LAMP1
Puncta numbers
Homozygous
Heterozygous
Wildtype
D
Control without Rapamycin
TEM
E
500nM Rapamycin
TEM
F
Relative individual mitochondria area
FTD3 Patient 1
Isogenic Control 1
FTD3 Patient 2
Isogenic Control 2
Homozygous
Heterozygous
Wildtype
G
Relative mitochondria / cytoplasm area
FTD3 Patient 1
Isogenic Control 1
FTD3 Patient 2
Isogenic Control 2
Homozygous
Heterozygous
Wildtype

Figure S4. Characterization of mitophagy and TEM ultrastructural analysis. Related to Figure 2-3. **A)** Representative ICC images of TOM20 and LAMP1 co-labelling. Scale bar, 25 µm. **B-C**) Quantifications of TOM20 and LAMP1 co-localization. Data represented in mean ± SEM. One-way ANOVA with Tukey multiple comparisons test; *p<0.05. **D-E)** Representative TEM images of astrocytes at 10 weeks of maturation. FTD3 astrocyte lines demonstrate an increase in electron-dense cargo-filled vesicles. Control without rapamycin treatment (**D**). 500nM rapamycin treatment **(E**). Examples of autophagosomes and autolysosomes are indicated with black arrows. (A= autophagosomes and L= autolysosomes), Scale bar=2µm. **F)** TEM quantitative analysis of relative individual mitochondria area. Data represented in mean ± SEM of three independent experiments. Unpaired t-test with Welch's. Significance differences are indicated with ***p < 0.001. **G)** TEM quantitative analysis of relative mitochondria to cytoplasm area ratio. Data represented as mean ± SEM. Unpaired t-test with Welch's. Significance differences are indicated with **p < 0.01, ***p < 0.001.

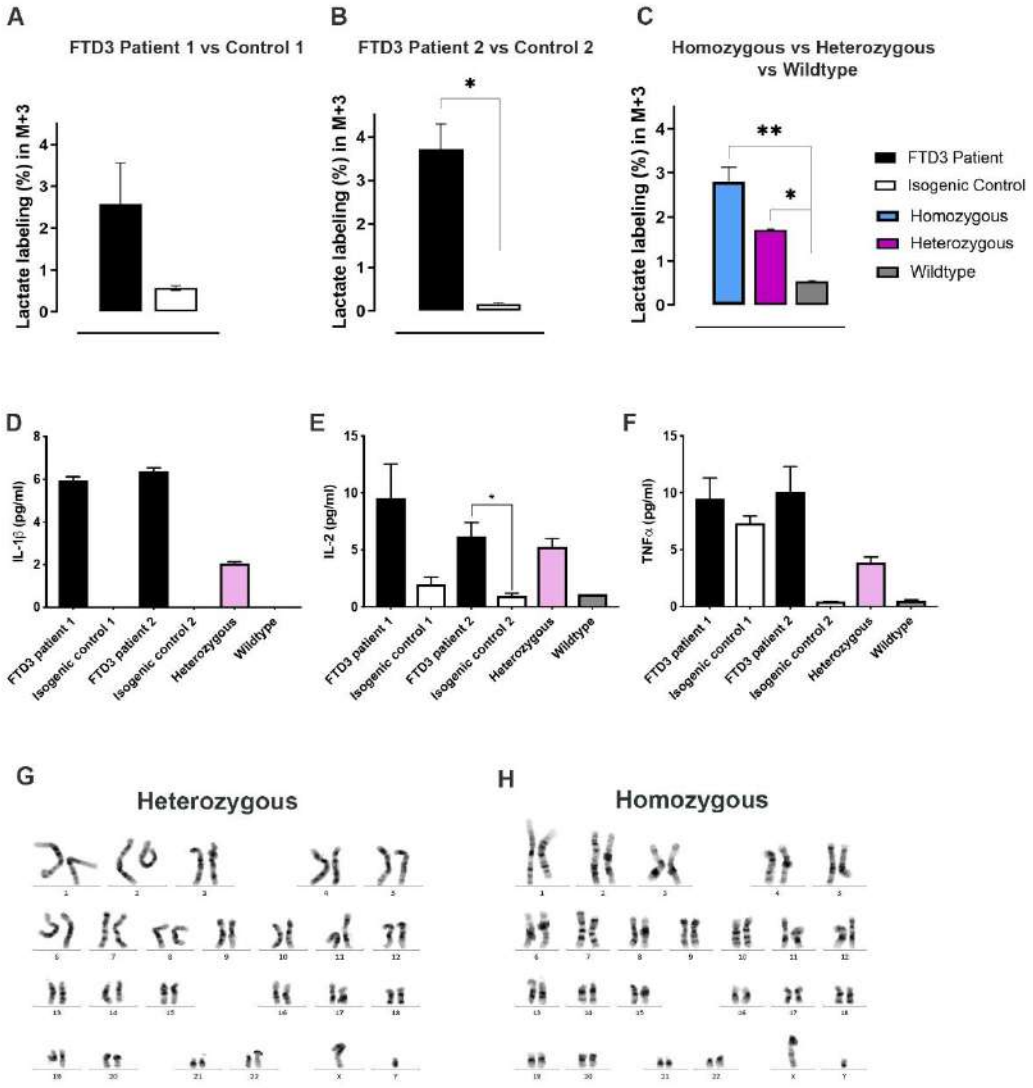

Figure S5. Metabolic Response to Glutamate/Glucose and Cytokine Profile. Related to Figure 4-5. A-C) Labeling percentage in lactate M + 3 in hIPSC-derived astrocytes after incubation with [U-^{13}C]glutamate and unlabeled glucose. **D-F)** Cytokine Profiling of IL-2, TNF α and IL-1β) of FTD3 related astrocyte lines compared to its controls. Data represented in mean ± SEM of three independent experiments. One-way ANOVA with Tukey multiple comparisons test; *p<0.05. **G-H)** Karyogram of heterozygous induced CHMP2B mutation (left) and homozygous induced CHMP2B mutation (right). Both cell lines expressed normal karyotype profile.

Supplemental Tables

Table S1. Overview of cell lines. Related to Figure 1.

hiPSC Line	Genotype	Karyotype	Pluripotency-associated Marker	Gender	References
H150 (FTD3 patient 1)	G/C 31449 in CHMP2B	Normal	+	M	Yu Zhang et al 2017
H151 (FTD3 patient 2)	G/C 31449 in CHMP2B	Normal	+	M	Yu Zhang et al 2017
H150 ISO (Isogenic control 1)	Gene corrected	Normal	+	M	Yu Zhang et al 2017
H151 ISO (Isogenic control 2)	Gene corrected	Normal	+	M	Yu Zhang et al 2017
K3 p53++	Homozygous mutant	Normal	+	M	Added to Figure S5
K3 p53+-	Heterozygous mutant	Normal	+	M	Added to Figure S5
K3 p53	Wild type	Normal	+	M	Mikkel Rasmussen et al 2014

Table S2. Selected differentially expressed genes. Related to Figure 3-5.
Subset of significantly differentially expressed genes detected by comparing patient-derived CHMP2B-mutant cell lines with Cas9-corrected controls. For a full list of significantly DE genes, see Table S3. Genes are grouped based on their association with processes, functions or characteristics of interest for the disease. Lists of genes related to each annotation were retrieved from one of the following sources as indicated: Gene Ontology (GO); WikiPathways; COMPARTMENTS; KEGG: literature (manually curated). For each gene, we report its name, Ensembl identifier, log2 fold change and adjusted P-value. Only significantly differentially expressed genes are reported (adjusted p-value <= 0.05, absolute log2 fold change >=1 and average of normalized read counts >=10). For genes grouped by associated compartment, we also provide the confidence score assigned in COMPARTMENTS; only genes with a confidence score >=3 is shown.

Table S3. Differentially expressed genes. Related to Figure 3-5.
List of significantly differentially expressed genes detected by comparing patient-derived CHMP2B-mutant cell lines with Cas9-corrected controls, and overrepresented terms obtained by comparing differentially expressed genes with expressed genes. For each differentially expressed gene, we report its name, Ensembl identifier, log2 fold change and adjusted P-value. Gene counts normalized by DeSeq2 in the sample are also provided. Only significantly differentially expressed genes are reported (adjusted p-value <= 0.05, absolute log2 fold change >=1 and average of normalized read counts >=10). Overrepresented terms were filtered by excluding redundant annotations (overlap between gene sets >= 50%).

Table S4. **Antibodies used for Immunocytochemistry, Western Blot and Primers used for RT-qPCR. Related to Figure 1-3 and 5.**

Immunocytochemistry				
	Antibody	**Antibody Registry* Identifier**	**Dilution**	**Company**
Astrocyte differentiation	rabbit anti-SOX9	AB_2665492	1:400	CST
	rabbit anti-GFAP	AB_10013382	1:1000	Dako
	rabbit anti-aquaporin4	AB_2274338	1:50	Abcam
	mouse anti-S100β	AB_882426	1:500	Sigma
Reactive Astrocyte	rabbit anti-LCN2	AB_10618739	1:200	Millipore
	mouse anti-TIA1	AB_2201439	1:100	Abcam
	rabbit anti-C3	AB_1240642	1:500	GeneTex
Autophagy pathway	rabbit anti-LC3B rabbit anti-LC3B	AB_881433 AB_881429	1:1000 1:2000	Abcam Abcam
	mouse anti-RAB7	AB_882241	1:1000	Abcam
	guinea pig anti-P62	AB_2687531	1:100	Progen
	mouse anti-LAMP1	AB_2296838	1:400	HB
Secondary antibodies	AF 488 donkey anti-rabbit IgG	AB_2534015	1:1000	TFS
	AF 488 donkey anti-guinea IgG	AB_2535788	1:2000	TFS
	AF 594 donkey anti-rabbit IgG	AB_2556547	1:2000	TFS
	AF 594 donkey anti-goat IgG	AB_2534105	1:1000	TFS
	AF 594 donkey anti-mouse IgG	AB_253578	1:1000	TFS
	AF 647 donkey anti-mouse IgG	AB_162542	1:1000	TFS
Western Blot				
	Antibody	**Antibody Registry* Identifier**	**Dilution**	**Company**
Primary antibodies	*rabbit anti-GAPDH	AB_9485, AB_307275	1:3000 1:3000	Abcam
	*mouse anti-GAPDH	AB_627678	1:4000	SCT
	rabbit anti-LC3B	AB_881429	1:3000	Abcam
	rabbit anti-C3	AB_1240642	1:10000	GeneTex
	mouse- LAMP1	AB_2296838	1:4000	HB
	rabbit-Phospho NF-Kb	AB_10827881	1:1000	CST
	rabbit- NF-Kb	AB_10859369	1:1000	CST
	mouse- Caspase 3	AB_781826	1:500	SCT
Secondary antibodies	IRDye® 800CW Donkey anti-Rabbit IgG (H + L)	AB_621848	1:15,000	LI-COR
	IRDye® 800CW Donkey anti-Mouse IgG (H + L)	AB_621847	1:15,000	LI-COR
	IRDye® 680LT Goat anti-Mouse IgG (H + L)	AB_10706161	1:20,000	LI-COR
	IRDye® 680LT Goat anti-Rabbit IgG (H + L)	AB_10706309	1:20,000	LI-COR
RT-qPCR primers				
Human Primers				
Gene Name	**Forward**	**Reverse**	**Concentration**	**Company**
OPA1	GGCGGAAGACCTCAAGAAAGT	GGCTGGACAAAAGACGTTGAT	10µM	OligoTagc
MFN1	CCAGAAAGTGGTGTGGCACT	GTTTTCACTGCTGACTGCGAG	10µM	OligoTagc
FIS1	GGTGCGGAGCAAGTACAATGA	CGTATTCCTTGAGCCGGTAGT	10µM	OligoTagc

MAP3K9	CTGGAACGGGAGCTCAACAT	TGGTGTCAACTGGATGGCTC	10µM	OligoTagc
DCN	CCCTCCTCCTTTCCACACCT	TTTTCACAACCAGGGAACCTTT	10µM	OligoTagc
GAS6	GACATAGACGAGTGCGCAGA	ACGGCAAGATGTCCTCACAG	10µM	OligoTagc
GAD1	GGGAACTAGCGAGAACGAGG	GGTATCGTACGTTGTGGGGC	10µM	OligoTagc
MT-ND2	TCATAGCAGGCAGTTGAGGC	GGTCGTGGTGCTGGAGTTTA	10µM	OligoTagc
IL17D	GAGTCCCCGGGTCTGGAT	GTGTGGTGGAAGGCACTGAG	10µM	OligoTagc
**GAPDH*	CTCTCTGCTCCTCCTGTTCGAC	TGAGCGATGTGGCTCGGCT	10µM	OligoTagc
Mouse Primers				
Gene Name	**Forward**	**Reverse**	**Concentration**	**Company**
mIl6	GATGCTACCAAACTGGATATAATC	GGTCCTTAGCCACTCCTTCTGTG	10µM	OligoTagc
mc3	ACCCCTTCATTCCTTCCACCT	CCTTACTGGCTGGAATCTTGATGG	10µM	OligoTagc
mLcn2	TCTGTCCCCACCGACCAATG	GGGGAGTGCTGGCCAAATAA	10µM	OligoTagc
mMap3k	ATCAGGAGATGAAGGCCTCAAG	AGGACTGGTTGGGTGAATGC	10µM	OligoTagc
mMfn1	CAGGGACGGAGTGAGTGTCC	GTTTCTGCCATTATGCACCTGGA	10µM	OligoTagc
mFis1	CTGGTGTCTGTGGAGGATCTGA	GAGCCTTTTCATATTCCTTGAGCC	10µM	OligoTagc
mOpa1	CTGCAGGTCCCAAATTGGTT	CTGCAGGTCCCAAATTGGTT	10µM	OligoTagc
MDcn	TTCCTACTCGGCTGTGAGTC	AAGTTGAATGGCAGAACGC	10µM	OligoTagc
mGad1	CCTTCGCCTGCAACCTCCTCGAAC	GCGCAGTTTGCTCCTCCCCGTTCTT	10µM	OligoTagc
mMt-nd2	AGGGATCCCACTGCACATAG	TGAGGGATGGGTTGTAAGGA	10µM	OligoTagc
mIl17d	GGGCGTACAGGATTTCCTAC	AGAGAAGACGGGTGTGCTG	10µM	OligoTagc
mGas6	AAAGGGCCAGAGTGAAGTGA	TTTTCCCGTTTACCTCCAGA	10µM	OligoTagc
*mGapdh	TGCACCACCAACTGCTTAG	GGATGACCTTGCCC	10µM	OligoTagc

AF, Alexa Fluor; TFS, Thermo Fisher Scientific Inc; HB, Hybridoma bank; CST, Cell Signalling Technology; IRDye, Infrared Dye, http://antibodyregistry.org/. GAPDH was used as reference gene, m=mouse.

Supplemental Experimental Procedures

Patient Information

In this study, we have used two unedited FTD3 hiPSC lines carrying CHMP2B mutation (referred to as FTD3 patient 1 and FTD3 patient 2 throughout the study), two corresponding CRISPR/Cas9 gene edited isogenic control hiPSC lines (referred to as Isogenic Control 1, Isogenic Control 2 throughout the study), one heterozygous mutant CHMP2B CRISPR/Cas9 induced hiPSC line (referred to as heterozygous throughout the study), one homozygous mutant CHMP2B CRISPR/Cas9 induced hiPSC line (referred to as homozygous throughout the study) and one corresponding healthy wildtype control hiPSC line (referred to as wildtype throughout the study). The detail information are added to the Table S1. All patients provided written informed consent. The studies were approved by the Ethics Committee of the Capital Region of Denmark (H-4-2011-157) institutional review board.

Generation of Cell Lines

hiPSCs were generated via episomal reprogramming (Addgene, 27077, 27078, 27080) from human dermal fibroblasts obtained from skin biopsies as described in (Zhang et al., 2017). The hiPSC lines were maintained on matrigel (BD Matrigel; 15535739, Stem Cell Technologies) in E8 culture media (05991, Stem Cell Technologies). The media was changed daily, and the cells were passaged every 5-7 days using 0.5 mM EDTA (B52, Thermo Fischer) according to the manufacturer's instructions. All hiPSC lines used in this study were characterized and published earlier in (Rasmussen et al., 2014; Zhang et al., 2017). Karyogram for the CRISPR/Cas9 induced heterozygous and homozygous CHMP2B hiPSC are presented in Figure S5.

CHMP2B Mice

Snap frozen brains of *CHMP2B*$^{wild\text{-}type}$ and *CHMP2B*$^{intron\ 5}$ were kindly provided by Adrian M. Isaacs. The mouse model was published earlier in (Ghazi-Noori et al., 2012). The mouse brain were 6 month-old at the time of study. Mouse brains were dissected and the cerebellum and brainstem were removed. Subsequently, one cerebral hemisphere was used for WB and the other for qPCR.

Neural Induction/ Generation of Neural Progenitor Cells

Neural progenitor cells (NPCs) were generated from each of the hiPSCs by dual SMAD inhibition, using LDN193189, an inhibitor of the BMP pathway (Selleck, S2618) and SB431542, a small molecule inhibitor of the TGFß pathway (Selleck, S1067) (Chambers et al., 2009). The neural differentiation was induced via 3D sphere-based method, according to the previously published method (Chandrasekaran et al., 2017).

Astrocyte Generation

We generated an efficient astrocyte differentiation protocol based on a modified version previously published (Shaltouki et al., 2013). To generate astrocytes, NPCs were first generated via 3D neural induction, where the neuronal rosettes were selected for astrocyte generation. NPCs were then plated at 70% confluence on matrigel in astrocyte differentiation media (ADM) media supplemented with 10 ng/ml of bFGF, 10 ng/ml of Activin A (Thermofisher, PHG9014) & 10 ng/ml Heregulin 1β (HRGβ1) (Peprotech, 100-03), and 200 ng/ml of Insulin Growth Factor-1 (IGF-1) (Peprotech, 100-11) (Shaltouki et al., 2013). Astrocyte maturation was achieved by passaging astrocyte progenitor cells (APCs) few times before plating (at least until passage 5, to switch from neurogenesis to gliogenesis). Enriched astrocyte progenitors were plated at a seeding density of 50.000 cells/cm^2 in astrocyte maturation media (AMM) medium supplemented with 10 ng/ml of Activin A, 10 ng/ml of HRGβ1, 200 ng/ml of IGF1, 1% sodium pyruvate (Thermofischer, 1136070), 2% heat inactivated and toxin free FBS (Invitrogen, 10100147) and 200 µM L-Ascorbic acid 2-phosphate (Sigma, A8960). The medium was changed every other day and cells were differentiated for 35+ days. The efficiency of terminal differentiation astrocytes was monitored for S100β, AQP4, and SOX9 by ICC. In the current study astrocyte progenitor cells were differentiated up to 7 weeks for astrocyte verification; and 10 weeks for the remaining assays: western blot (WB), transmission electron microscopy, cytokine profiling, RNA-seq, qPCR and metabolic assay.

Rapamycin Treatment

To evaluate the rescuing effect of rapamycin on autophagy impairments, cell cultures were treated with rapamycin (R8781, Sigma) before performing the following assays. At 10 weeks of maturation, cell cultures were induced with 200 nM and 500 nM rapamycin in AMM medium to visualize any concentration

dependencies of rapamycin and incubated at 37°C for 24 hours and subsequently fixed for TEM. For ICC, cell cultures were induced with 200 nM and 500 nM of rapamycin at 10 weeks of maturation and incubated for 37°C for 24 hours followed by fixation. Control cell lines were kept in AMM media as reference.

Immunocytochemistry and Confocal Microscopy
Cells were cultured on 0.17 µM glass coverslips coated with matrigel. Cell cultures were fixed in 4% paraformaldehyde (PFA) for 20 min, room temperature (RT), washed 3 times with PBS and permeabilized (0.2% Triton X-100 in PBS; 20 min). After blocking for 30 minutes (at RT in 5% donkey serum) the cells were incubated with primary antibodies (Table S4, ICC panel) overnight at 4°C. On the following day, the isotype specific secondary antibodies (Table S4, ICC panel) were applied (1 hour at RT). Samples were washed in PBS and stained with DAPI (Sigma-Aldrich, D9542) to label the nuclei of the cells. Samples were visualized on a confocal microscope equipped with a Leica TCS SPE microsystem controlled by LAS X software (v 2.0.0.14332).

Puncta Quantification
Puncta (small spherical fluorescence points) were counted by analysing fluorescent images using the Puncta Analyzer plugin of the Image J software. Fifteen different randomly chosen fields from three independent experiments were counted by an independent investigator in a double blinded approach.

MitoTracker ® Assay
Cells for MitoTracker® Red CMXRos (Molecular Probes, M7512) analyses were cultured on 0.17 µM glass coverslips coated with matrigel. Cells were incubated with 100 nM MitoTracker® in DMEM/F-12 medium for 15 min at 37 °C, followed by fixation in 4% PFA in PBS for 15 min, permeabilization in 0.5% Triton X-100 in PBS for 15 min and incubation with DAPI for 7 min at RT. In between each step the samples were washed 3 times in PBS. After the last wash, the glass coverslips were mounted with mounting media and sealed onto slides. Images were acquired by laser scanning confocal microscopy Leica TCS SPE microsystems controlled by LAS X software (v 2.0.0.14332). The analysis was performed on 10 weeks matured astrocyte samples.

Quantitative qPCR
RNA was extracted using RNeasy® Plus Mini Kit (Qiagen, 74134) according to the manufacturer's protocol. cDNA was synthesized from 1 µg of total RNA (from the human samples) in 20 µL reaction using iScript™ cDNA synthesis Kit (BIO-RAD, 1708890). After synthesis, the cDNA was diluted four times with double distilled water and were subjected to PCR amplification with primers (Table S4, primer panel). Likewise for mouse brain samples, 1 µg of CHMP2B mouse brain RNA from three mice per genotype at 6 months of age was synthesized. Quantitative real-time PCR (qPCR) reactions were done in triplicates using the FastStart Lightcycler 480 SYBR Green I Master (Roche, 04707516001) on Lightcycler® 480 real-time PCR system (Roche, Switzerland) for both human and mouse.

RNA-Sequencing Library Preparation
For RNA sequencing, two unedited FTD3 hiPSC lines carrying CHMP2B mutation (FTD3 patient 1, FTD3 patient 2), two corresponding CRISPR/Cas9 gene edited isogenic control hiPSC lines (Control 1, Control 2) and one heterozygous mutant CHMP2B CRISPR/Cas9 induced hiPSC line (heterozygous) were employed for gene expression analysis. The heterozygous astrocytes were used for variant-aware off-target evaluation. The quality of extracted RNA was checked on Agilent 2100 Bioanalyzer system using RNA 6000 nano chip and reagents. All the RNA samples had RIN value > 6. QC passed RNA samples were further used to construct the RNA libraries with TruSeq RNA Library Prep Kit using manufacturer's protocol. The libraries were quantified using Qubit 3.0 and Agilent 2100 Bioanalyzer system using DNA HS chips. qPCR was performed for precise concentration of the libraries and all the libraries were pooled in equimolar concentrations. The pooled libraries were sequenced on Illumina HiSeq 2500 sequencing platform with 1X100 single end reads.

RNA-Sequencing Data Analysis and Functional Association of Differentially Expressed Genes
Transcript reads were pre-processed by trimming low-quality 3' ends and adapter sequences with cutadapt v1.13 (Martin, 2011) (phred quality threshold=30). Reads shorter than 90 nt were removed and all remaining reads were trimmed at the 3' end to a common length of 90 nt. Reads matching rRNAs were extracted with

BBDuk v38.22 (BBDuk) (minimum covered fraction = 0.5, kmer size = 31) based on the annotations available in SILVA v119.1 (Quast et al., 2013). Pre-processed reads were mapped to the human genome (hg38) with HISAT2 v2.1.0 (Kim et al., 2019), resulting in an average of 33,84 M uniquely mapping reads per sample. Alignments were inspected with Samtools v1.9 mpileup function (Li et al., 2009) to confirm the presence/absence of the CHMP2B mutation (Chr3:87,253,711 G>C) and of the silent edits introduced by template-directed Cas9 editing (Chr3:87,253,729 A>C, Chr3:87,253,732 T>G). Non-chimeric reads were assigned to genomic features annotated in GENCODE v29 (Frankish et al., 2019) with feature Counts (Subread v1.6.3) (Liao et al., 2014). Differential expression analysis was carried out with DESeq2 v1.22.2 (Love et al., 2014) by comparing n = 4 patient-derived CHMP2B mutated cell lines (time points 5 and 10 weeks) with their CRISPR/Cas9 gene-corrected isogenic controls. Time point information was introduced in the DESeq2 formula as batch effect. Genes with Benjamin-Hochberg adjusted P-value (Wald test) <= 0.05, absolute log2 fold change >= 1 and mean of normalized counts >= 10 were considered significantly differentially expressed in the comparison between the two groups.
Functional and compartmental labelling was done for the differentially expressed genes by grouping them based on functional or subcellular compartment annotation downloaded from AmiGO v2 (Blake et al., 2015) (GO:0000266, GO:0008053, GO:0000422, GO:0019646, GO:0006119, GO:1900016, GO:1900017, GO:0034351, GO:0034352, GO:0090141), Wikipathways (Slenter et al., 2018) (WP3941, WP408, WP4459, WP534), COMPARTMENTS (Binder et al., 2014) (GO:0005768, GO:0005764, GO:0005739), KEGG (Kanehisa, 2000) (hsa04064, hsa04668), or from manually curated literature [For details refer: Table S2 & S3]. For subcellular compartment annotation, only genes with a confidence cut-off of at least 3 were considered. Additional functional associations between differentially expressed genes with a confidence cut-off of at least 0.8 were retrieved from STRING v11 (Szklarczyk et al., 2019) through the StringApp v1.5 (Doncheva et al., 2019) and further visualized and annotated in Cytoscape v3.7.1 (Shannon et al., 2003). Functional enrichment analysis of differentially expressed genes was computed with the StringApp, setting as background all the genes expressed in our samples (mean of normalized counts >= 10). Results were filtered by excluding annotations showing high redundancy with a more statistically significant annotation (overlap between gene sets >= 50%).

Metabolic Mapping

The culture medium was removed and the cells were washed with PBS (37°C). Cell cultures were subsequently incubated for 90 min at 37ºC in the presence of 2.5 mM [U-^{13}C] glucose or 2.5 mM [1,2-^{13}C] acetate plus 2.5 mM unlabeled glucose (Frandsen et al., 1989). The concentrations of substrates were chosen based on previous studies (Aldana et al., 2017). After the incubation, the medium was collected and the cells were washed with cold PBS (4°C), lysed and extracted with 70% ethanol. The cells were scraped off the dish and centrifuged at 20,000 g for 20 min (4ºC) to separate the soluble extract (supernatant) from the insoluble components (pellet). Cell extracts were lyophilized and reconstituted in water for subsequent biochemical analyses. The cell extracts were separated and metabolites were mapped using a gas chromatograph (Agilent Technologies 7820A chromatograph, J&W GC column HP-5MS, parts no. 19091S-433) coupled to a mass spectrometer (Agilent Technologies, 5977E). The isotopic enrichment was calculated according to (Biemann, 1962). Data are presented as labelling (%) of M+ X, where M is the mass of the unlabeled molecule and X is the number of labelled C-atoms in a given metabolite.

Transmission Electron Microscopy

For transmission electron microscopy (TEM) the cells were fixed at 10 weeks of maturation with 3% glutaraldehyde (Merck, 1042390250) in 0.1 M mNa-phosphate buffer, pH 7.4, post-fixed in 1% osmium tetroxide in 0.1 M Na phosphate buffer, dehydrated stepwise in a graded ethanol series, and embedded in Epon (TAAB, T031). Semi-thin (2 µM) sections were cut with glass knifes on an ultramicrotome (Leica Ultracut, Leica Microsystems, Wetzlar, Germany), stained with 1% toluidine blue O (Millipore, 1159300025) in 1% Borax (LabChem, LC117101). Ultra-thin (50 nm to 70 nm) sections were sectioned with a diamond knife (Jumdi, 2 mm) on an ultramicrotome (Leica Ultracut), contrasted with 2% uranyl acetate (Polyscience, 21447) and lead citrate (Merck, 1073980100), and examined using a Philips CM100 transmission electron microscope operating at 60 kV. Photographs were taken using Olympus Morada 11-megapixel camera and iTEM software (Olympus).

Multiplex Array

Cytokine concentrations were measured in duplicates using the MESO QUICKPLEX SQ 120 imager (MSD) with the software DISCOVERY WORKBENCH 4.0 and the data were normalized to protein content. Only values above detection level and with a CV value below 25 were included.

Real-time assessment of mitochondria respiration function via Seahorse XFe96

Oxygen consumption rate (OCR) was measured using a Seahorse XFe96 Extracellular Flux Analyzer (Agilent, USA). Human APCs from FTD3 patient cell lines and from knock-in cell lines carrying the CHMP2B mutation were seeded in a Seahorse 96-well cell culture microplate at a density of 12,000 cells/well for 10 weeks until they reach astrocytic maturation. On the day of the assay, the cells were washed twice and changed to Seahorse assay medium (unbuffered DMEM (pH 7.4) supplemented with 2.5 mM glucose and 3 mg/L phenol red) and the cells were equilibrated for 10 min at 37°C in a CO2-free incubator. The reagents used to test mitochondrial function were pH adjusted to 7.4. The OCR measurement cycle consisted of 3-min mix and 3-min measurement of the oxygen level. Mitochondrial function assessment was initiated by three baseline OCR measurement cycles. These were followed by the sequential injection of: (a) the inhibitor of ATP synthase, Oligomycin (2 µM final concentration); (b) the uncoupling agent, Carbonyl cyanide 4- (trifluoromethoxy) phenylhydrazone (FCCP, 1 µM); (c) a mixture of the inhibitors of mitochondrial complexes I and III, Rotenone (0.5 µM) and Antimycin A (0.5 µM) with three OCR measurement cycle in between each injection and three final measurement cycles. Oxygen consumption rates were automatically recorded and calculated by the software, Wave (Agilent). Subsequent to the Seahorse analysis, in order to normalize the data, the protein content was measured for each well using the Pierce assay with bovine serum albumin as standard. Results are expressed as mean values ± SEM from 12 wells/plate obtained in triplicate for each condition. Basal respiration was determined by subtracting non-mitochondrial respiration (minimum measurement after rotenone/antimycin injection) from the last measurement obtained before oligomycin injection; maximal respiration, measurement obtained after FCCP injection; for obtaining the oxygen consumption associated to ATP production, the measurement after oligomycin injection was subtracted from the last measurement before oligomycin injection.

CellROX (CellROS)

ROS were detected in cells (5×10^5) stained at 37°C for 30 min with 5 µM (cell lines) CellROX green, according to the manufacture instruction. After staining, the cells were washed and analysed with FACS analyzer.

Co-culture with Astrocyte Condition Media

To assess the effects of neurite outgrowth, condition media obtained from FTD3 related astrocytes and controls were cultured on wild type neurons for 5 days, then cells were fixed using 4% PFA for immunocytochemistry. Wild type neurons were kept in neuronal differentiation media as reference. Neurite length was assessed using neurite tracer software of Image J. The analysis was carried out blinded by an independent investigator.

Western Blot

CHMP2B mouse brain tissues were lysed in tPER™ tissue protein extraction reagent (Thermo Fisher Scientific, 78510) and cell from FTD3 astrocytes and controls were lysed in mPER™ mammalian protein extraction reagent (Thermo Fisher Scientific, 78501) containing protease inhibitor (Complete tablets, Roche Diagnostics 04693116 001) and phosphatase inhibitors (PhosSTOP tablets, Roche Diagnostics 04906845001). 10 µg of protein were separated by NuPAGE™ Novex™ 4-12 % Bis-Tris mini gel (Thermo Fisher Scientific, NP0322BOX) and transferred from gel to membranes by XCell II™ Blot Module (Invitrogen, EI9051). The membranes were incubated with primary antibodies solution overnight at 4°C (refer details and dilutions in supplement table s4, western blot panel). After washing, the membranes were incubated with conjugated secondary antibodies for 1½ hour at RT. All the secondary antibodies are detailed in supplement table S4, western blot panel. Immunoblots were developed with LI-COR Developer Odyssey® FC Imager with 2 minutes at channel 800 and 2 minutes at channel 700 and data was processed using the Image Studio Lite Version 5.2. Expression levels of LC3B, LAMP1, C3, NF-kB and pNF-kB were normalized to GAPDH. In general, we also looked into caspase 3 activity via WB.

Neurite Length Analysis

The cells were plated for neurite outgrowth. At the time of plating, the pre-differentiated neurons (Day 0 of terminal differentiation) appeared spherical in shape with no apparent neurite outgrowth. After 24 hours post-plating, thin neurites began to emerge from the cell bodies of the cells. After 5 days of terminal differentiation in ACM, the neurons were quantified via image analysis as described in (Pool et al., 2008).

Statistical Analysis

For all experiments, data are presented as mean ± standard errors of the mean (SEM) of three independent experiments. Statistical analysis were made in GraphPad Prism 7.03. Statistical analyses were determined using Student's t test or by one way ANOVA with a Tukey's post-test or by two-way ANOVA with Bonferroni post hoc test for differences of mean between each groups. Statistical significance were labelled in figures as (*$p < 0.05$, **$p < 0.01$, ***$p < 0.001$, ****$p < 0.0001$).

Supplemental References

Aldana, B.I., Zhang, Y., Lihme, M.F., Bak, L.K., Nielsen, J.E., Holst, B., Hyttel, P., Freude, K.K., and Waagepetersen, H.S. (2017). Characterization of energy and neurotransmitter metabolism in cortical glutamatergic neurons derived from human induced pluripotent stem cells: A novel approach to study metabolism in human neurons. Neurochem. Int. *106*, 48–61.

BBDuk BBDuk Guide - DOE Joint Genome Institute.

Biemann, K. (1962). The Application of Mass Spectrometry in Organic Chemistry: Determination of the Structure of Natural Products. Angew. Chemie Int. Ed. English *1*, 98–111.

Binder, J.X., Pletscher-Frankild, S., Tsafou, K., Stolte, C., O'Donoghue, S.I., Schneider, R., and Jensen, L.J. (2014). COMPARTMENTS: unification and visualization of protein subcellular localization evidence. Database (Oxford). *2014*, bau012.

Blake, J.A., Christie, K.R., Dolan, M.E., Drabkin, H.J., Hill, D.P., Ni, L., Sitnikov, D., Burgess, S., Buza, T., Gresham, C., et al. (2015). Gene Ontology Consortium: going forward. Nucleic Acids Res. *43*, D1049-56.

Chambers, S.M., Fasano, C.A., Papapetrou, E.P., Tomishima, M., Sadelain, M., and Studer, L. (2009). Highly efficient neural conversion of human ES and iPS cells by dual inhibition of SMAD signaling. Nat. Biotechnol. *27*, 275–280.

Chandrasekaran, A., Avci, H.X., Ochalek, A., Rösingh, L.N., Molnár, K., László, L., Bellák, T., Téglási, A., Pesti, K., Mike, A., et al. (2017). Comparison of 2D and 3D neural induction methods for the generation of neural progenitor cells from human induced pluripotent stem cells. Stem Cell Res. *25*, 139–151.

Doncheva, N.T., Morris, J.H., Gorodkin, J., and Jensen, L.J. (2019). Cytoscape StringApp: Network Analysis and Visualization of Proteomics Data. J. Proteome Res. *18*, 623–632.

Frandsen, A., Drejer, jørgen, and Schousboe, A. (1989). Direct Evidence That Excitotoxicity in Cultured Neurons Is Mediated via N-Methyl-D-Aspartate (NMDA) as well as Non-NMDA Receptors. J. Neurochem. *53*, 297–299.

Frankish, A., Diekhans, M., Ferreira, A.-M., Johnson, R., Jungreis, I., Loveland, J., Mudge, J.M., Sisu, C., Wright, J., Armstrong, J., et al. (2019). GENCODE reference annotation for the human and mouse genomes. Nucleic Acids Res. *47*, D766–D773.

Ghazi-Noori, S., Froud, K.E., Mizielinska, S., Powell, C., Smidak, M., Fernandez De Marco, M., O'Malley, C., Farmer, M., Parkinson, N., Fisher, E.M.C., et al. (2012). Progressive neuronal inclusion formation and axonal degeneration in CHMP2B mutant transgenic mice. Brain *135*, 819–832.

Kanehisa, M. (2000). KEGG: Kyoto Encyclopedia of Genes and Genomes. Nucleic Acids Res. *28*, 27–30.

Kim, D., Paggi, J.M., Park, C., Bennett, C., and Salzberg, S.L. (2019). Graph-based genome alignment and genotyping with HISAT2 and HISAT-genotype. Nat. Biotechnol. *37*, 907–915.

Li, H., Handsaker, B., Wysoker, A., Fennell, T., Ruan, J., Homer, N., Marth, G., Abecasis, G., and Durbin, R. (2009). The Sequence Alignment/Map format and SAMtools. Bioinformatics *25*, 2078–2079.

Liao, Y., Smyth, G.K., and Shi, W. (2014). FeatureCounts: An efficient general purpose program for assigning sequence reads to genomic features. Bioinformatics *30*, 923–930.

Love, M.I., Huber, W., and Anders, S. (2014). Moderated estimation of fold change and dispersion for RNA-seq data with DESeq2. Genome Biol. *15*.

Martin, M. (2011). Cutadapt removes adapter sequences from high-throughput sequencing reads. EMBnet.Journal *17*, 10.

Pool, M., Thiemann, J., Bar-Or, A., and Fournier, A.E. (2008). NeuriteTracer: A novel ImageJ plugin for automated quantification of neurite outgrowth. J. Neurosci. Methods *168*, 134–139.

Quast, C., Pruesse, E., Yilmaz, P., Gerken, J., Schweer, T., Yarza, P., Peplies, J., and Glöckner, F.O. (2013). The SILVA ribosomal RNA gene database project: Improved data processing and web-based tools. Nucleic Acids Res. *41*.

Rasmussen, M.A., Holst, B., Tümer, Z., Johnsen, M.G., Zhou, S., Stummann, T.C., Hyttel, P., and Clausen, C. (2014). Transient p53 Suppression Increases Reprogramming of Human Fibroblasts without Affecting Apoptosis and DNA Damage. Stem Cell Reports *3*, 404–413.

Shaltouki, A., Peng, J., Liu, Q., Rao, M.S., and Zeng, X. (2013). Efficient Generation of Astrocytes from Human Pluripotent Stem Cells in Defined Conditions. Stem Cells *31*, 941–952.

Shannon, P., Markiel, A., Ozier, O., Baliga, N.S., Wang, J.T., Ramage, D., Amin, N., Schwikowski, B., and Ideker, T. (2003). Cytoscape: A software Environment for integrated models of biomolecular interaction networks. Genome Res. *13*, 2498–2504.

Slenter, D.N., Kutmon, M., Hanspers, K., Riutta, A., Windsor, J., Nunes, N., Mélius, J., Cirillo, E., Coort,

S.L., Digles, D., et al. (2018). WikiPathways: a multifaceted pathway database bridging metabolomics to other omics research. Nucleic Acids Res. *46*, D661–D667.
Szklarczyk, D., Gable, A.L., Lyon, D., Junge, A., Wyder, S., Huerta-Cepas, J., Simonovic, M., Doncheva, N.T., Morris, J.H., Bork, P., et al. (2019). STRING v11: Protein-protein association networks with increased coverage, supporting functional discovery in genome-wide experimental datasets. Nucleic Acids Res. *47*, D607–D613.
Zhang, Y., Schmid, B., Nikolaisen, N.K., Rasmussen, M.A., Aldana, B.I., Agger, M., Calloe, K., Stummann, T.C., Larsen, H.M., Nielsen, T.T., et al. (2017). Patient iPSC-Derived Neurons for Disease Modeling of Frontotemporal Dementia with Mutation in CHMP2B. Stem Cell Reports *8*, 648–658.